UAV Icing: Intercycle Ice Effects on Aerodynamic Performance

Joachim Wallisch[1,2], Richard Hann[1,2]

1 Norwegian University of Science and Technology (NTNU), Department of Engineering Cybernetics, UAV Icing Lab, Trondheim, Norway

2 UBIQ Aerospace, Trondheim, Norway

Abstract

Atmospheric in-flight icing poses a challenge to all aircraft including unmanned aerial vehicles (UAVs). Aircraft should avoid icing conditions unless they have ways of mitigating the negative effects of icing, e.g., if they are equipped with an ice protection system (IPS). When de-icing systems are used, a certain amount of ice is allowed to accumulate before it is removed. This intercycle ice deteriorates the aerodynamics by reducing the lift, adding mass, and increasing the drag. This study combines the energy that is required to compensate for the added drag of intercycle ice shapes with the energy required for a wing IPS and compares the energy needs for different IPS operations. Two different kinds of intercycle ice shapes are simulated numerically using FENSAP-ICE, one ice shape that would accrete on an unprotected wing and one ice shape that would accrete when using a parting strip, a continuously heated element at the leading edge. The results show that both intercycle ice shapes deteriorate the aerodynamic performance of the airfoil significantly compared to a clean airfoil. Additionally, the results show that the aerodynamics deteriorate fastest in the initial stages of ice accretion, likely caused by fast horn growth and a fast transition from laminar to turbulent flow. The aerodynamic performance is combined with energy requirements of electrothermal de-icing tests in an icing wind tunnel. The results show that de-icing with a parting strip is more energy-efficient than de-icing without a parting strip and anti-icing. In addition, it is found that the energy required for the IPS on a wing is significantly larger than the energy required to compensate for the added intercycle drag. Considering these results during the development and operation of an IPS will help to improve the range and endurance of UAVs in icing conditions.

Introduction

The operational envelope of unmanned aircraft is limited by severe weather conditions that pose a significant challenge for the aircraft. Atmospheric in-flight icing, also known as in-cloud icing, is one of these potentially dangerous weather conditions [1]. Icing occurs when an aircraft flies through a cloud that contains supercooled droplets - droplets that are in a liquid state although their temperature is below the freezing point. When supercooled droplets hit unprotected surfaces of the aircraft, they will start to freeze. These ice accretions can have several negative effects on aircraft performance. Icing on the engines or propellers reduces the thrust of the aircraft [2-4], ice on antennas or sensors can make them behave faultily [5], and ice accretions on wings deteriorate the wing aerodynamics [6]. Deteriorated wing aerodynamics appear through different effects. The drag is increased significantly, while the lift is reduced. Additionally, the stall angle and maximum lift coefficient are reduced. This increases the stall speed of the aircraft and can potentially lead to the aircraft operating in stall before the stall alarm goes off because of the reduced stall angle. Overall, the effect of icing leads to an increase in energy required for the aircraft to operate and, in the worst case, can cause the aircraft to crash [5]. Hence, aircraft might require mitigation against the negative effects of icing to operate continuously in icing conditions.

One mitigation action against icing is the use of ice protection systems (IPS). IPS are typically divided into three categories: Chemical, mechanical, or thermal IPS [7]. Chemical IPS use fluids to depress the freezing point of water and keep the ice from freezing. In the case of mechanical IPS, the surface is deformed rapidly to shed the ice from the surface. The deformation can be achieved in different ways, e.g., with pneumatic boots or electromagnetic impulses. When thermal IPS are used, the surface temperature of the protected areas is heated to be above the freezing point of water. Additionally, the operation of IPS can be divided into anti-icing and de-icing. If an IPS is operated in anti-icing mode, the surface is always protected, and no ice accretion is allowed on the protected surfaces. IPS that operate in de-icing are only activated periodically to remove the ice that has accreted while the IPS was not active [7,8].

Icing can be a challenge for all types of aircraft. In particular for unmanned aerial vehicles (UAVs) [9], often also called uncrewed aerial vehicles, unmanned aerial systems (UAS), remotely piloted aerial systems (RPAS), or drones. UAVs exist in many different sizes and shapes, ranging from a few centimeters to almost 20 meters of wingspan, and can either be rotorcraft or fixed-wing aircraft [10]. To reduce the scope of work, this study focuses on icing on small fixed-wing UAVs. This term applies to fixed-wing UAVs with a wingspan of a few meters and a maximum take-off weight of less than 25 kg. While mature IPS exist for manned aircraft [7], research is still required to develop efficient and reliable IPS for UAVs. This is also because small fixed-wing UAVs show several differences from manned aircraft when it comes to icing [1]. For example, the Reynolds numbers in cruise flight are typically one or two orders of magnitude lower for UAVs than for manned aircraft. Since lower Reynolds numbers result in more severe icing [11,12], UAVs face more risk when flying in icing conditions than manned aircraft. Other differences between UAVs and manned aircraft are the flight altitude, the weight, the propulsion system, and the degree of autonomy. Additionally, the amount of energy that is available on a manned aircraft is typically much larger than the available energy on a UAV. Hence, energy efficiency is more important for UAVs than it is for manned aircraft. The differences between unmanned and manned aircraft also cause the need for special research on IPS for UAVs because IPS that are in use for manned aircraft might not be suitable for UAVs, at least not without optimizations.

Previous research on IPS for UAVs was often looking at thermal IPS [13–15]. It has been found that the operation of thermal IPS as an anti-icing system requires more energy than the operation of the IPS as a de-icing system [13]. Adding a parting strip to the de-icing system improves the energy efficiency of thermal IPS even further [13]. The parting strip is a heating element located at the leading edge of the wing and is heated continuously to prevent ice

accretion at the leading edge. When the other heating zones are activated, not all ice must be melted but the ice will shed when the water film between the wing surface and the remaining ice is of sufficient size [8,16]. This is because the aerodynamic forces push the ice from the wing.

One shortcoming of previous research on the energy efficiency of electrothermal IPS for UAVs was their sole focus on the energy required for the IPS [13,14]. However, during the operation of de-icing systems, ice is allowed to accrete on the wing – the so called intercycle ice. These ice accretions reduce the lift and the stall angle, add mass to the aircraft, and increase the drag of the aircraft. As a result of the increased drag, also the required thrust to maintain constant flight conditions is increased. Hence, the aircraft will also require more energy for the propulsion unit while operating in icing conditions. According to the authors' knowledge, no study exists that considers the energy required for the IPS and the aerodynamic influence of intercycle ice on the UAV. One parametric study was performed for an electrothermal IPS on the wing of a manned aircraft considering the IPS power as well as the aerodynamics [17]. However, that study also looked on both aspects separately and did not combine the energies for the IPS and the propulsion unit.

Since the available energy and maximum power of small UAVs are limited, quantifying the additional power and energy required is important for the safe operation of a UAV in icing conditions. Additionally, knowing the total energy required for de-icing and thrust generation in icing conditions would be a valuable addition to existing path planners in icing conditions [18,19].

This paper intends to fill the gap and combine the energy needs of the IPS and of maintaining constant flight through icing conditions. The aerodynamic performance of intercycle ice shapes is investigated using numerical simulations. Lift and drag are captured over the time of ice accretion for a wing without an IPS and for a wing with a running parting strip. Simulations are performed for different temperatures and liquid water contents (LWC). A comparison between the different ice shapes and a clean airfoil is performed. A simple estimation model is introduced to calculate the additional thrust and power required for the aircraft to compensate for the drag increase. The added power requirement is combined with the energy used to de-ice a wing in experiments [13] to develop a single number that describes the energy efficiency of certain ice protection strategies. A comparison between the energy efficiency of anti-icing, conventional de-icing, and parting strip de-icing is presented based on the energy efficiency at different temperatures and LWCs. The results of this study are relevant for developers of electrothermal IPS and users of UAVs with electrothermal IPS since the study increases knowledge about the energy required for flight in icing conditions for different IPS operations.

Methods

The structure of this paper is divided into two parts. First, the aerodynamic performance of an airfoil with intercycle ice shapes is evaluated using numerical simulations. In the second part, the aerodynamic degradation of airfoils is translated into additional thrust and power requirements. These power requirements are combined with experimental data of the required energy for an IPS to compare the overall energy need of different IPS solutions.

The Numerical Method

All numerical simulations used meshes that were generated using the meshing tool of ANSYS Fluent version 2022 R2. This tool was selected because it is also implemented for remeshing of multi-shot simulations with ANSYS FENSAP-ICE [20]. Hence, the mesh settings can be kept the same for all meshes that are used during a multi-shot icing simulation. The meshes were generated as 2.5-D meshes, i.e., all meshes consist of only one cell in the spanwise direction. This allows having a finer resolution of the mesh in the leading edge region without increasing the number of cells or the computational requirements significantly. Three-dimensional effects cannot be captured using 2.5-D meshes but are considered negligible for this study.

All meshes have a farfield diameter of eighty times the chord length. This farfield size should be sufficient to remove any possible influence of the farfield. The surface of the airfoil is meshed in an unstructured manner with varying cell sizes along the chord. The highest mesh resolution is chosen at the leading edge since most droplets will impinge in this vicinity. The mesh is of a hybrid type, consisting of prism layers close to the walls to capture the boundary layer and triangles outside the boundary layer. Because the size of the prism layers depends on the mesh spacing on the airfoil's surface, a thicker prism layer can be found downstream of the leading edge. This can be seen in Figure 1, a close-up view of the leading edge area of the final clean mesh that was the result of a mesh study.

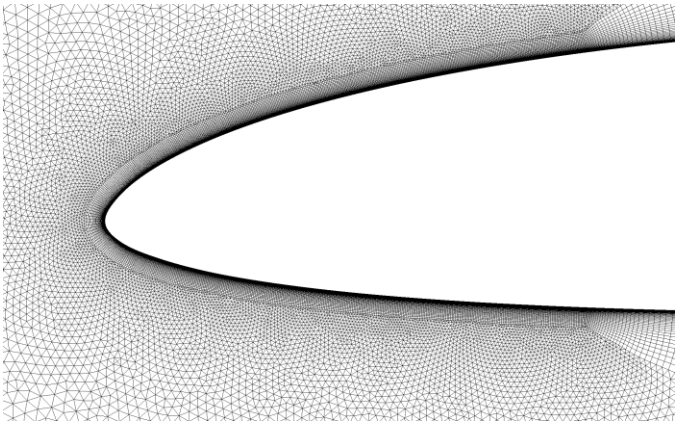

Figure 1: A close-up view of the hybrid mesh around the leading edge of the clean airfoil. The prism layer expands downstream because of larger cell sizes on the airfoil's surface.

The numerical simulations are performed using the computational fluid dynamics (CFD) software ANSYS FENSAP-ICE version 2022 R2. FENSAP-ICE is a commercial CFD software developed for icing simulations [21]. The code performs sequential simulations of the airflow, the droplet impingement, and the ice accretion to generate the results. Additionally, FENSAP-ICE allows using a multi-shot approach for ice accretion simulations. This means that the total duration of ice accretion is divided into smaller intervals. After each interval, the grid is updated using automatic remeshing to adjust to the new ice shape. FENSAP-ICE allows using the meshing tool of ANSYS Fluent to generates a new mesh. The same mesh settings were chosen for the remeshing as for the initial clean mesh. The mesh around an iced airfoil is shown in Figure A. 1 and discussed later. Previous studies proved that simulating ice shapes with FENSAP-ICE on UAVs generates good results [22,23].

Numerical simulations of ice accretion typically assume fully turbulent flow [24]. However, the ice shapes that are generated with a

parting strip will have a clean area around the leading edge. Thus, parts of the flow might be laminar rather than turbulent and it was decided to consider the flow to be transitional. Prior to this study, simulations were performed to find the best model at predicting transition for cases at low Reynolds number. As a result, the k-ω-SST turbulence model was selected in combination with an intermittency transition model [25] and was used for all simulations presented in this study.

Since the parting strip will prevent droplets that hit the heated area from freezing, the ice shapes will be influenced more significantly by runback water. To simulate runback water more accurately, gravity was included in the calculations of the airflow, the droplet impingement, and the droplet freezing. Additionally, all simulations were performed with a constant ice density of 917 kg/m^3. All flow simulations are performed using a second order streamline upwind artificial viscosity model. An overview of all numerical settings can also be found in Table A. 1.

Validation of the Numerical Method

To validate the numerical method of simulating intercycle ice shapes with a parting strip gap, the results were compared against the results of an experiment. A wing equipped with an electrothermal IPS was tested in the icing wind tunnel at the Technical Research Centre of Finland (VTT) in Helsinki [13,26]. The RG-15 airfoil was used since it was also the airfoil for the numerical simulations. The protected wing part had a chord length of 0.35 m and was tested at an air temperature of −5 °C, an LWC of 0.44 g/m^3, and a median volume diameter (MVD) of 24 µm. The airspeed was 25 m/s, and the angle of attack (AOA) of the airfoil was 0°. The ice shape after four minutes was captured using photogrammetry and compared to numerical simulations [27].

To simplify icing simulations, the droplets are normally assumed to be monodisperse although it has been shown that using droplet size distributions can improve the agreement with experimental results [28]. Since the simulation of intercycle ice shapes on UAVs with a parting strip is a novel method, it was also investigated whether the difference between monodisperse droplet sizes and the Langmuir-D droplet size distribution [29] was significant.

Simulation of Different Icing Regimes

The regulations for aircraft approval specify atmospheric icing conditions in 14 CFR Part 25, Appendix C [30]. If a manufacturer wants to certify an aircraft for flight in icing conditions, it must be proven that the aircraft can cope with the conditions specified in the regulations. For this study, four different conditions were selected from Appendix C continuous maximum icing conditions. The temperatures of −2 °C, −5 °C, and −10 °C were chosen since they are representative of glaze, mixed, and rime ice accretions for UAVs [23,31]. An MVD of 20 µm was found to be worst for typical UAV flight conditions [32] and hence selected for this study. To investigate the influence of droplet size, one simulation at −5 °C with a larger MVD was conducted as well. All icing conditions of the four different simulations are summarized in Table 1.

Table 1. The icing conditions of the different simulations. All conditions are chosen from the continuous maximum icing conditions. The parting strip heat flux is chosen sufficiently large to keep the heated area ice-free.

Regime	Temperature, °C	LWC, g/m^3	MVD, µm	Parting strip heat flux, kW/m^2
Rime	−10	0.42	20	7.2
Mixed	−5	0.53	20	3.8
Mixed	−5	0.13	40	3.6
Glaze	−2	0.59	20	1.6

All CFD simulations and experiments were conducted on an RG-15 airfoil. Because the RG-15 airfoil was developed for low Reynolds numbers [33], it is a good airfoil for small fixed-wing UAVs. A chord length of 0.3 m is chosen for the comparison of different icing regimes. The cruise speed of the aircraft is chosen as 25 m/s. Hence, the Reynolds number for the initial simulations is 600,000. These values were chosen since they are typical for small fixed-wing UAVs [10]. The AOA during all ice accretion simulations was kept constant at 4°. This is an appropriate angle of attack for the selected flight conditions to generate enough lift to compensate for the mass of a small UAV of 25 kg.

Flight through a cloud as specified in the continuous maximum icing conditions with a speed of 25 m/s takes 1290 s or 21.5 min. For all four ice accretion simulations, 15 shots were used. Every shot was 90 seconds long, except for the first shot which was only 30 seconds. Choosing time steps with a different length would have implications on the results that will be discussed in the discussion section. The shorter first shot is chosen to simulate the initial ice roughness without having to specify a roughness value. FENSAP-ICE uses an analytical model to calculate the surface roughness caused by ice accretion [34,35]. This roughness value is based on the development of water beads on the surface.

Two different kinds of ice accretion simulations were performed. The first one is an ice shape on an unheated airfoil. This case describes the ice shapes that accrete when flying in icing conditions without a proper IPS, without detecting icing, or when using a conventional de-icing system without a parting strip. The second type of simulated ice shapes is ice accretions while heating a parting strip. To simulate the parting strip, a heat flux is assigned to a small portion of the leading edge. Using FENSAP-ICE, the maximum heat flux required for a running wet anti-icing system can be simulated. This heat flux is rounded conservatively and assigned to the leading edge covering an additional 1.5 mm from the leading edge towards the suction and the pressure sides. Additionally, the heat flux is assumed to decrease linearly to 0 W/m^2 for an additional 0.5 mm downstream. The resulting heat flux distribution is shown in Figure 2 and the heat fluxes used for different conditions are included in Table 1.

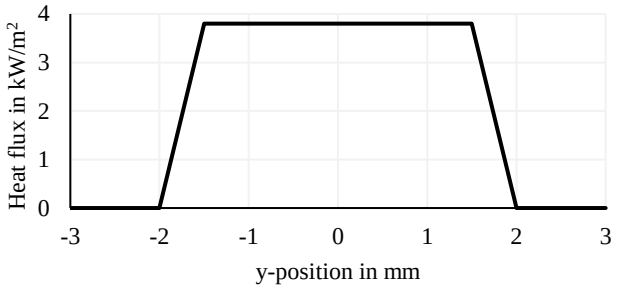

Figure 2: An exemplary heat flux distribution for a parting strip simulation.

The ice accretions for different icing regimes can be compared regarding the ice shapes and the aerodynamic performance of the iced airfoil. To increase the comparability between different icing regimes, the final angle of attack sweep is performed at −5 °C for all ice shapes.

The Required Energy for Flight in Icing Conditions

The degraded aerodynamics of iced airfoils have several implications on the flight performance of the aircraft. First, the lift coefficients of iced airfoils are smaller than the lift coefficient of a clean airfoil. This requires the aircraft to increase its speed or the angle of attack to produce enough lift. The required changes are considered negligible for this study. In addition, the mass of the ice increases the mass of the aircraft and forces the aircraft to generate more lift to compensate the mass increase. However, the ice mass is considered negligible during the following calculations. The influence of neglecting the reduced lift coefficient and the added ice mass in this study will be re-evaluated in the discussion section. For this study, the focus is solely on the increased drag of iced airfoils compared to the drag of clean airfoils. The aircraft requires more thrust to compensate for the added drag. This will result in higher energy needs for the propulsion unit.

To perform a more thorough investigation of the energy efficiency of different IPS methods and operation modes, the added power needs of the iced airfoil must be considered in addition to the IPS power. This study combines the required IPS power found by Hann et al. [13] with drag data calculated using the numerical methods presented in the previous section.

The required IPS power was investigated experimentally in an icing wind tunnel with a wing based on the RG-15 airfoil with a chord length of 0.45 m. The conditions in the icing wind tunnel were kept constant at the LWC of 0.44 g/m^3, the MVD of 24 µm, the velocity of 25 m/s, and the AOA of 0°. Hence, the Reynolds number for this part of the study is 900,000.

The IPS tests were performed at temperatures of −2 °C, −5 °C, and −10 °C. Different IPS operation methods were compared regarding their shedding time and the energy that was required for the IPS until the ice had shed. The tested methods were anti-icing, conventional de-icing, and de-icing with a parting strip. More information on the experimental setup can be found in [13].

The CFD simulations were done using the same conditions as in the experimental campaign. Additionally, the same numerical settings as presented before were used with the following exceptions. The mesh was scaled to the bigger chord length but the resolution at the leading edge was kept constant to have a good resolution of the ice shapes. Since the ice accretion times in the experimental campaign were significantly shorter than specified in the Appendix C icing conditions, the durations of the icing shots were adjusted as well. The two first ice shots were simulated for 30 seconds and all following shots for 60 seconds. Different ambient temperatures result in different heat flux requirements to keep the leading edge area ice-free. The CFD simulations were done using a heat flux of 1.3 kW/m^2 for a temperature of −2 °C, 3.1 kW/m^2 for −5 °C, and 5.8 kW/m^2 for −10 °C.

Calculating how much energy is required to compensate for the drag increase of the iced airfoils, takes multiple steps. First, the drag

$$D = 0.5\rho u^2 c_d A \tag{1}$$

is calculated [36]. For all cases, the air density ρ is assumed to be 1 kg/m^3. This air density would be expected for a UAV flying at a height of 2,000 m or 6,500 ft. The velocity u is kept constant at the cruise speed of 25 m/s. The drag coefficient c_d of the iced airfoils is calculated in the numerical simulations. The reference area A would normally consist of the airfoil chord and the combined span of both wings. However, since also the IPS power depends on the protected span, all values are normalized by the span and the reference area depends only on the chord length. For all following calculations, only the difference in drag ΔD between the iced airfoil and the clean airfoil is used.

The UAV must increase the thrust by the same amount as the drag increases to maintain steady-state flight. This increase in thrust ΔT results in an increase in required engine power

$$\Delta P_{Engine} = \frac{\Delta T\, u}{\eta_{Prop}\eta_{Engine}} = \frac{\Delta D\, u}{\eta_{Prop}\eta_{Engine}} \tag{2}$$

that also depends on the propeller efficiency η_{Prop} and the efficiency of energy generation η_{Engine}. During the following calculations, the propeller efficiency is assumed as 0.75 [3,37,38]. Additionally, it is assumed that the propeller is powered by an electric motor with an efficiency of 0.8 for the entire unit [37].

The energy ΔE_{Engine} that was required to generate the additional thrust during the time interval t can be calculated by integration:

$$\Delta E_{Engine}(t) = \int_0^t \Delta P_{Engine}\, dt \tag{3}$$

Since the drag increase is only calculated at distinct points in time, the trapezoidal rule is used to calculate the integral numerically. To compare the required energy for different ice accretion times more easily, a time-averaged energy is calculated

$$\Delta \bar{E}_{Engine}(t) = \frac{\Delta E_{Engine}(t)}{t}. \tag{4}$$

The energy required for the IPS until the ice has shed is provided as energy per heated area and per time. Hence, it must only be transformed to the correct size to be combined with the energy required for the drag compensation. As explained before, the span can be removed from the calculations since it is only a multiplier for both, the IPS energy and the energy for the thrust. Hence, the experimental values given in [13] are only multiplied by the length of the heating zones in chordwise direction, i.e., 15 cm for the wing that was tested in the icing wind tunnel.

Results

The result section is divided into three parts. First, the numerical method is validated. Second, the influence of intercycle ice shapes on the aerodynamic performance will be evaluated for different icing regimes. Finally, the power requirements for thrust and ice mitigation are combined into the overall energy requirement of a UAV flying in icing conditions.

Validation of the Numerical Method

To verify the method, a numerical ice shape is compared to an experimental ice shape. A good agreement between the two shapes can be found as can be seen in Figure 3. The experimental ice shape appears slightly larger than the numerical ice shape regarding the horn size, the icing limit on the pressure side, and the amount of runback ice on the pressure side. However, these differences are in line with previous studies [12,23]. Additionally, when simulating both ice shapes using CFD, the aerodynamic coefficients only show minor differences prior to stall, as can be seen in Figure A. 2 in the appendix. Hence, the numerical method is considered validated for this study.

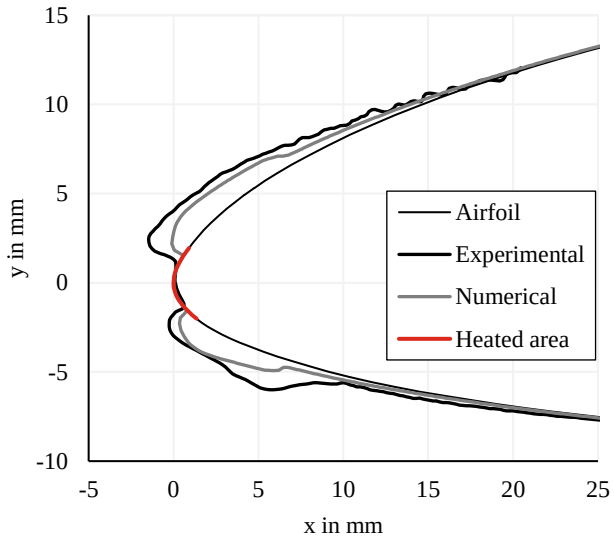

Figure 3: The comparison of an experimental intercycle ice shape and an ice shape simulated numerically at −5 °C after 240 s of icing with LWC = 0.44 g/m^3. Airspeed 25 m/s, 0.35 m chord, MVD 24 µm, AOA 0°.

The comparison between a monodisperse droplet cloud and a cloud with the Langmuir-D droplet size distribution was performed for the mixed icing regime at −5 °C, 0.53 g/m^3 LWC, and 20 µm MVD over a duration of 1110 s and with a chord length of 0.3 m. As can be seen in Figure 4, the difference between the two intercycle ice shapes is insignificant. A more detailed analysis showed that the icing limit on the pressure side is slightly further downstream for the Langmuir-D distribution because of the higher inertia of the bigger droplets in the distribution. The icing limits are important during the design of an IPS since the goal is to protect all or most of the areas where ice can accrete. However, the influence of the droplet size distribution on the ice shapes and the aerodynamic performance is negligible for this study and hence, all following simulations are performed using a monodisperse cloud.

The ice shapes shown in Figure 4 look significantly different than the ice shapes shown in Figure 3. This is because the shapes in Figure 4 are the result of 1110 s of icing duration, while the duration for the shapes in Figure 3 was only 240 s. The longer icing duration results in a significantly larger ice thickness, particularly visible in the horn region. The bigger horns also catch more droplets, preventing them from impacting further downstream. As a result, the ice shapes look slightly more streamwise for longer icing durations.

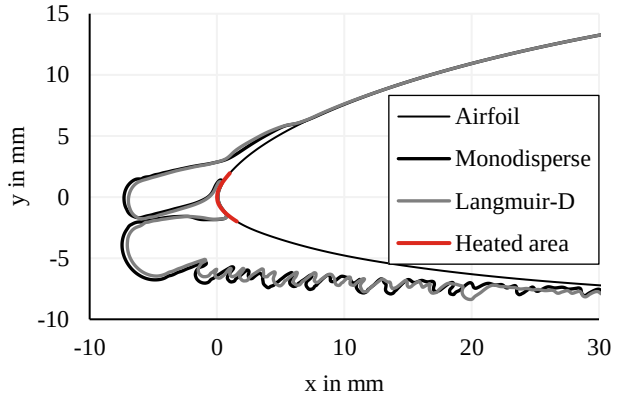

Figure 4: The difference between a monodisperse droplet distribution and the Langmuir-D droplet size distribution for −5 °C, 0.53 g/m^3 LWC, and 20 µm MVD after 1100 s icing duration. Airspeed 25 m/s, chord length 0.3 m, AOA 4°.

Simulation of Different Icing Regimes

The following part will present the different ice shapes for runs with and without parting strip for flight in icing conditions at different temperatures. Additionally, the resulting aerodynamic coefficients will be compared between the two ice shapes and to a clean airfoil. All runs considered an icing duration of 1290 s in Appendix C continuous maximum conditions and had a chord length of 0.3 m.

The purpose of a parting strip is to divide the ice into an upper and a lower part with a gap in between since this results in faster shedding. The effect of the parting strip and the divide of the ice accretion in two parts can be seen in the resulting ice shapes. The ice shapes that result from a flight in Appendix C continuous maximum conditions at −5 °C are shown in Figure 5.

The parting strip results in an ice shape with two big horns while the ice shape without a parting strip has only one horn. The maximum ice thickness is slightly larger for the ice shape without a parting strip. This is likely related to the wider ice horn of the unheated case that catches more droplets compared to the thinner horns for the parting strip case. However, the upper horn of the parting strip ice shape extends further downstream than the ice shape on an unprotected airfoil. This is probably due to the increased amount of runback water caused by the parting strip preventing impinging droplets to freeze in the leading edge area. In total, the ice mass per span is almost the same, 0.132 kg/m for the fully-iced case and 0.134 kg/m for the parting strip case.

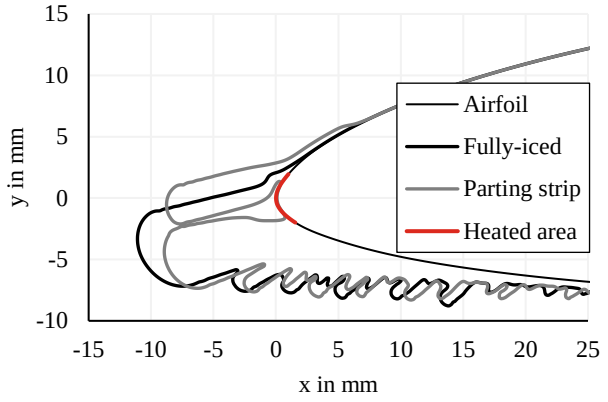

Figure 5. The ice shapes with and without parting strip after 1290 seconds of flight in icing conditions at −5 °C, 0.53 g/m^3 LWC, and 20 µm MVD. Airspeed 25 m/s, 0.3 m chord, AOA 4°.

An interesting characteristic of the parting strip ice shape is that the two horns grow towards each other. As can be seen in Figure 6, the upper horn is angled further towards the bottom than the lower horn. As a result, the gap between the two horns decreases for longer ice accretion times. The reason for the different angles of the two horns is related to the angle of attack. Because of the positive angle of attack, the stagnation point is located on the lower ice horn. Hence, parts of the flow are guided towards the suction side and the upper horn. Thus, more droplets will hit the lower side of the upper horn, resulting in the highest collection efficiency there.

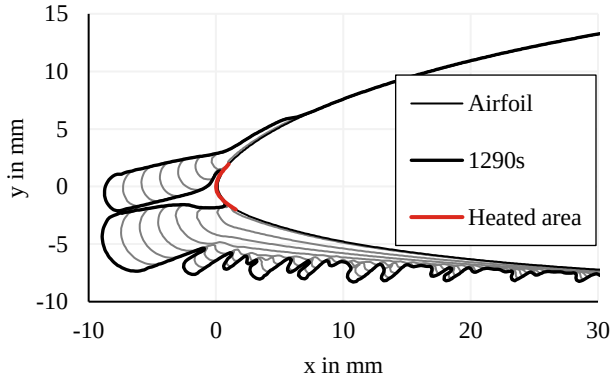

Figure 6: The development of the parting strip ice shapes at −5 °C, 0.53 g/m^3 LWC, and 20 µm MVD for different durations of ice accretion. The first ice shape line is for 30 s of ice accretion and the difference between two ice shapes is 180 s of ice accretion. Airspeed 25 m/s, 0.3 m chord, AOA 4°.

The effect of the two horns on the aerodynamics can be seen when comparing the lift and drag coefficients plotted in Figure 7. Both ice shapes generate less lift than the clean airfoil. The decrease in lift coefficient at 4° AOA compared to the clean airfoil is 8% for the parting strip shape and 5% for the ice shape on the unprotected airfoil. The reduction in lift coefficient becomes worse for higher angles of attack. Additionally, the maximum lift coefficient is reduced significantly compared to the clean case, by 20% for the parting strip case and 12% for the fully-iced shape. While the stall angle of the normal ice shape is not reduced compared to the clean case, stall happens 1° earlier for the ice shape generated with the parting strip. In general, the parting strip ice shape is the worst in lift coefficient for all angles of attack, but also the full ice shape has a significantly reduced lift coefficient compared to the clean case.

The same observation can be made for the drag coefficient. Both ice shapes are characterized by larger drag coefficients than the clean airfoil, even for moderate angles of attack. At 4° AOA, the parting strip shape increases the drag coefficient by 148% compared to the clean airfoil, while the fully-iced shape increases the drag coefficient by 124%. Because of the earlier stall, also the drag coefficients at large angles of attack are worse for both ice shapes than for the clean airfoil. The differences between the two different ice shapes are minor except for the stalled region where the shape with a parting strip has a larger drag coefficient. The aerodynamics of the parting strip ice shape is likely the worst because of the two horns since they display a less streamlined airfoil geometry than the fully-iced case. In addition, the airflow on the suction side of the airfoil has a separation bubble extending further downstream for the ice shape with parting strip, as can be seen in Figure A. 3 in the appendix.

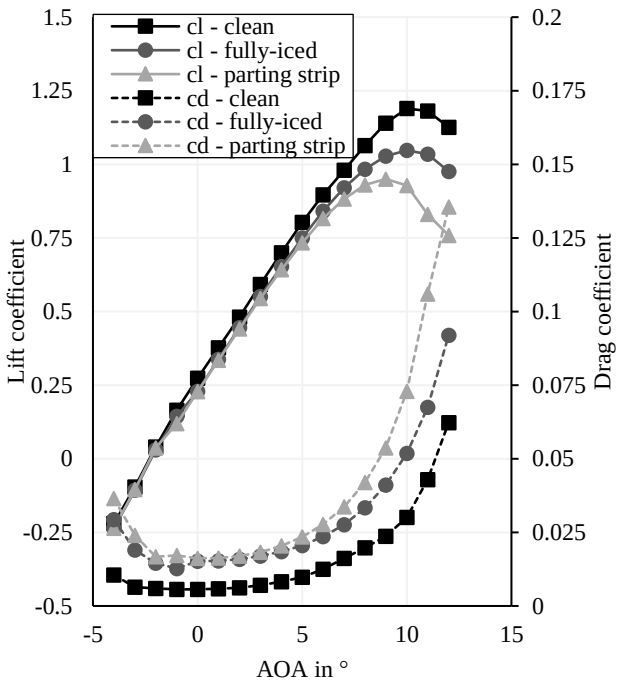

Figure 7. The plots of the lift coefficient c_l and the drag coefficient c_d for a clean airfoil, an iced airfoil without a parting strip, and an iced airfoil with a parting strip. The coefficients of the iced airfoils are for 1290 seconds long icing encounters at −5 °C, 0.53 g/m^3 LWC, and 20 µm MVD with an AOA of 4°. Airspeed 25 m/s, 0.3 m chord.

One goal of the study presented in this paper is to find optimum intercycle times. Hence, the temporal development of the aerodynamic performance in icing conditions must be evaluated. Figure 8 shows how the lift and the drag coefficient for 4° AOA change over time.

The first observation is that aerodynamic degradation happens faster for the ice shape with the parting strip. The drag coefficient almost doubles within 120 seconds for the ice shape with a parting strip, while the same drag is only reached after about twice the time for the normal ice shape. The difference is even bigger for the lift coefficient. Most of the reduction in lift coefficient happens within the first 120 seconds for the parting strip simulations. The lift coefficient degrades much more linearly for the normal ice shape,

and it never becomes as small as the lift coefficient of the parting strip ice shape is after 120 seconds.

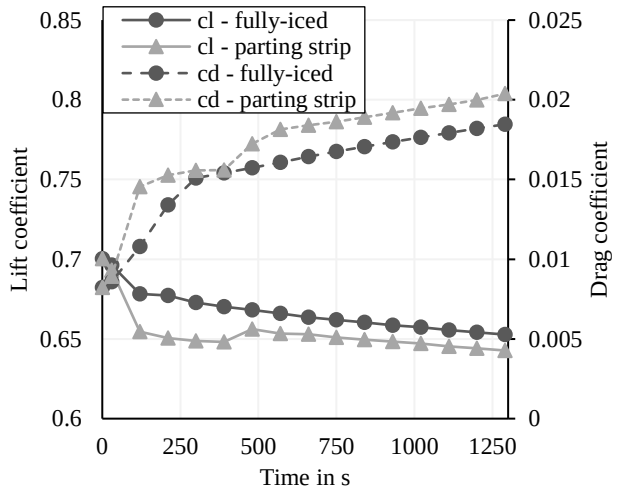

Figure 8. The lift coefficient c_l and the drag coefficient c_d for a fully-iced airfoil and an iced airfoil with a parting strip for different durations of icing encounters at −5 °C, 0.53 g/m³ LWC, and 20 µm MVD. Airspeed 25 m/s, 0.3 m chord, AOA 4°.

The reason for the faster degradation in the parting strip case is related to the geometry. The full ice shape after 120 seconds of ice accretion shows only minor differences from the clean airfoil and hence only a small aerodynamic degradation. However, the ice shape with the parting strip gap has already two distinct horns after 120 seconds as can be seen in Figure 9. These horns disturb the flow and reduce the aerodynamic performance more significantly.

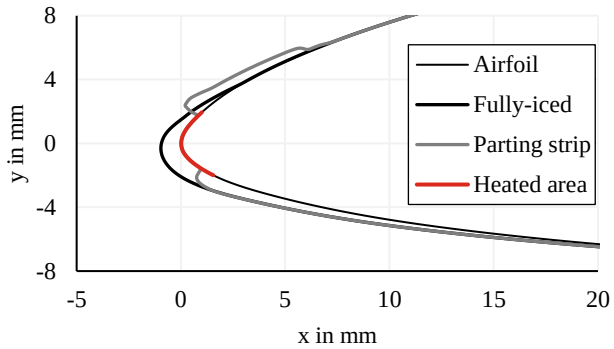

Figure 9: The ice shapes with and without parting strip after 120 seconds of flight in icing conditions at −5 °C, 0.53 g/m³ LWC, and 20 µm MVD. Airspeed 25 m/s, 0.3 m chord, AOA 4°.

The simulations also show that the degradation is most severe within the initial period of ice accretion. After about 200 seconds for the parting strip case and about 400 seconds for the normal ice shape, the increase in drag coefficient is much smaller than in the initial period. This is likely related to the geometry that has developed its general shape after a short time of ice accretion. While the ice shapes still increase in size, the geometry does not change much anymore and hence, also the degradation of the performance coefficients happens more slowly. In addition, the flow becomes turbulent after a short time, increasing the drag significantly. Another observation is the difference in relative change between the lift and drag coefficient.

While the drag coefficient for the parting strip case increases by 250% over the entire duration, the lift coefficient is only reduced by less than 10%.

Significant differences exist for the intercycle ice shapes at different ambient temperatures, as can be seen in Figure 10. The biggest differences are related to the angle of the ice horns and their thickness. For the warmest temperature, −2 °C, the horns grow at a significant distance from each other and are smaller than the horns for the other two cases. With colder temperatures, the horns grow more towards each other and become larger. This is likely related to higher freezing fractions for colder temperatures. As a result, more droplets freeze instantaneously where they impinge for colder temperatures. Since the horns catch the most droplets, the horns grow much bigger in cold temperatures. For warmer temperatures, more water will not freeze instantaneously but flow downstream resulting in a wider angle between the two horns. In the case of −10 °C, the horns grow so far towards each other, that they eventually hit, resulting in a closed ice gap. Because the remeshing happens only on the outer shape of the geometry, the resulting ice shape appears to be completely closed in the CFD. However, there would be air trapped inside the ice shape in reality. The intercycle ice shapes that would accrete on an unprotected wing in the same icing conditions are shown in Figure A. 4.

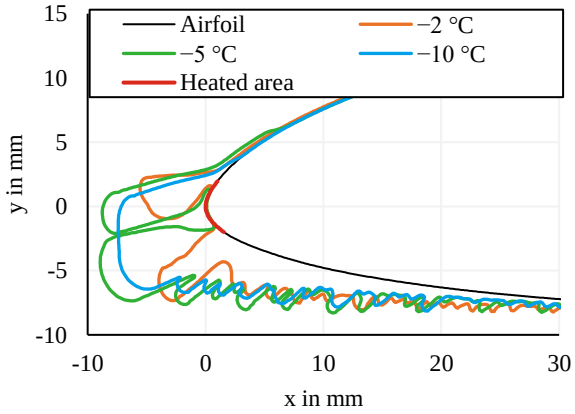

Figure 10: The intercycle ice shapes with parting strip for different temperatures after 1290 seconds of ice accretion in continuous maximum conditions for an MVD of 20 µm. Airspeed 25 m/s, 0.3 m chord, AOA 4°.

Plots of the lift and drag coefficients at −2 °C and −10 °C for different angles of attack and ice accretion times are included in the appendix. In general, the same characteristics are found for all ambient temperatures. The lift of intercycle ice shapes is decreased moderately for low angles of attack while the drag coefficient is increased more significantly for all angles of attack. Additionally, the parting strip leads to a deteriorated stall behavior for all temperatures. The biggest difference exists between the fully-iced cases that show decreasing aerodynamic performance for warmer temperatures.

A comparison of the lift and drag coefficients for the final intercycle ice shapes for various angles of attack is shown in Figure 11. The results are comparable to what has been found for ice shapes without parting strip gaps [32]. All ice shapes show a slight reduction in lift coefficient in the linear region with the biggest reduction for the warmest temperature of −2 °C. At 4° AOA, the lift coefficient is reduced by 7% for −10 °C compared to a clean airfoil, by 8% for −5 °C, and by 9% for −2 °C. The degradation is more significant in the stall region with higher penalties for warmer temperatures. While

stall happens at 10° AOA for a clean airfoil, the stall angle is reduced by 1° for −10 °C and −5 °C, and by 2° for −2 °C. The maximum lift coefficient is reduced by 17% for −10 °C compared to a clean airfoil, by 20% for −5 °C, and by 29% for −2 °C.

While the lift reduction in the linear region is small, the drag increase of the iced airfoils is significant for all angles of attack. Because of the earlier stall of iced airfoils compared to clean airfoils, the drag coefficient of iced airfoils becomes much worse for higher angles of attack. The increase in drag coefficient is worse for warmer temperatures. At 4° AOA, the drag coefficient is increased by 155% for −10 °C compared to a clean airfoil, by 148% for −5 °C, and by 216% for −2 °C.

The reason for the worse aerodynamic performance in the stall region for ice shapes at warmer temperatures might be related to the horn geometry. The ice shape at −2 °C has a large distance between the horns and bigger horn angles. This might cause the flow to separate more easily and could result in stall if the flow is no longer able to reattach to the airfoil. The ice shapes at colder temperatures have either no remaining gap or only a very small one. Additionally, the horns grow more in the flow direction. While these ice shapes still show significant deterioration of the airfoil aerodynamics, they might have less influence on flow separation and reattachment, and hence change the stall behavior less than the ice shape at −2 °C.

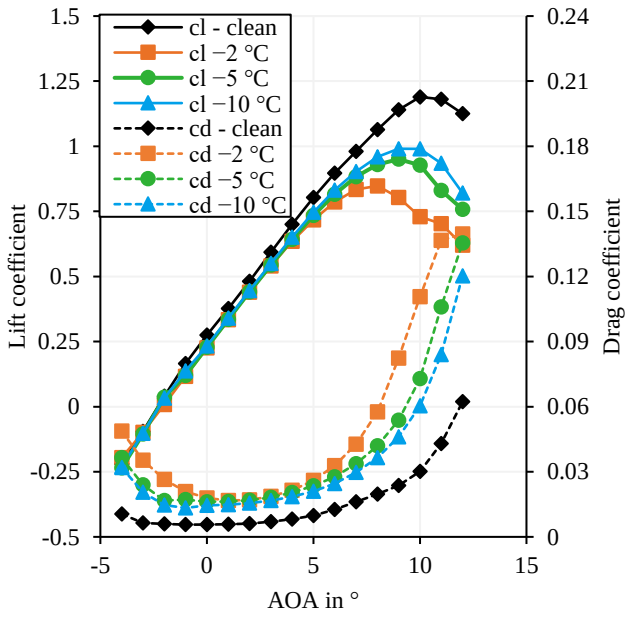

Figure 11: The lift and drag coefficients of the final intercycle ice shapes with parting strip plotted over the angle of attack. The coefficients of the iced airfoils are for 1290 seconds long icing encounters in continuous maximum conditions for 20 µm MVD at different temperatures while flying with an AOA of 4°. Airspeed 25 m/s, 0.3 m chord.

Comparing the lift and drag coefficients after different ice accretion durations shows a more diverse result than the angle of attack sweep. As shown in Figure 12, aerodynamic degradation happens faster in colder temperatures. While the ice shapes at −2 °C and −5 °C show only minor differences in lift and drag coefficient to a clean case after 30 seconds, the ice shape at −10 °C already caused significant increases in drag coefficient and reductions in lift coefficient. This is likely because the ice shape at −10 °C already has horns that grow normal to the airfoil resulting in significant alterations of the airflow.

The ice shapes at warmer temperatures do not have horns yet but a more streamlined geometry, although the LWC is larger for warmer temperatures. The difference in ice shapes for different ambient temperatures is likely related to the different freezing fractions for different temperatures. The larger freezing fraction at cold temperatures results in the immediate freezing of droplets where they hit the airfoil and a faster growth of ice horns.

However, as explained before, the aerodynamic performance of the final ice shapes is worse for warmer temperatures. It can be seen from Figure 12 that the lift and drag coefficients change more slowly after approximately 120 seconds for colder ambient temperatures. This is likely related to the lower LWC for colder temperatures, resulting in less ice accreted in total.

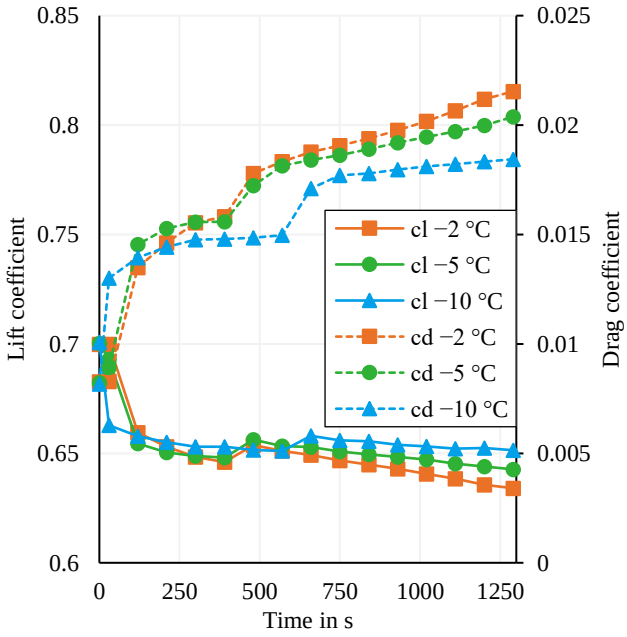

Figure 12: The lift and drag coefficients for different ambient temperatures over ice accretion duration for the intercycle ice shapes with parting strip. All ice accretions are in continuous maximum conditions for 20 µm MVD. Airspeed 25 m/s, 0.3 m chord, AOA 4°.

The ice shape generated at −5 °C for the larger MVD of 40 µm shows two distinct differences compared to the smaller MVD of 20 µm. First, as can be seen in Figure 13, the ice shape is much smaller for the larger droplet diameter. This is because the LWC is four times smaller for the larger droplets. Second, the ice shape generated with larger droplets shows a wider gap between the two horns. However, as was shown in Figure 6, the gap between the two horns typically closes when more ice has accreted. Hence, the wider gap size might be rather an effect of less ice accretion than of the larger MVD.

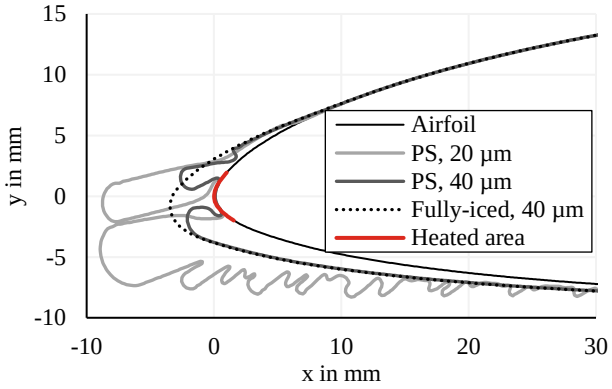

Figure 13: The intercycle ice shapes for different droplet diameters after 1290 seconds of ice accretion in continuous maximum conditions at −5 °C. The parting strip shapes are indicated with "PS". Airspeed 25 m/s, 0.3 m chord, AOA 4°.

The aerodynamic coefficients of the cases with smaller and larger droplet sizes, plotted in Figure 14, also show two significant differences. First, the ice shape with larger droplets has less influence on the lift and drag coefficients for moderate angles of attack. This is likely related to the lower LWC for large droplet sizes and the smaller ice shape that results from the lower LWC. However, despite resulting in a smaller ice shape, the conditions with 40 µm MVD result in a worse stall behavior. The stall angle and the maximum lift coefficient are reduced compared to the conditions with 20 µm MVD. This is likely related to the increased gap size between the two horns for the case with larger droplets. Indeed, also when looking at reduced accretion times for the lower MVD, it can be found that the stall angle and the maximum lift coefficient are reduced more significantly than for the full ice accretion time, see Figure A. 9.

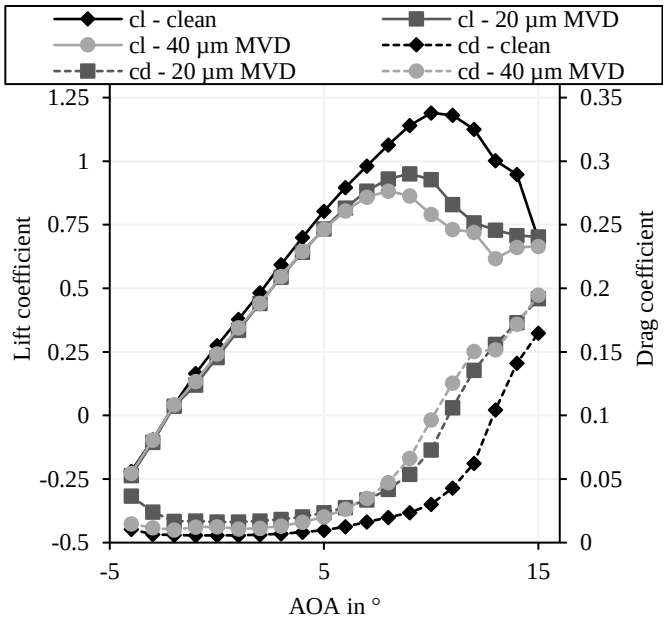

Figure 14: The lift and drag coefficients of the final intercycle ice shapes with parting strip after flight in continuous maximum conditions for 1290 s at −5 °C for different droplet sizes with an AOA of 4°. Airspeed 25 m/s, 0.3 m chord.

The Required Energy for Flight in Icing Conditions

Because of the availability of experimental data, the investigation of the required energy is done on a wing with a chord length of 45 cm instead of 30 cm. All runs are performed at the same LWC of 0.44 g/m^3 and MVD of 24 µm, while the parting strip heat flux is adjusted for every temperature to keep the leading edge ice-free. When comparing the CFD ice shapes for these conditions after 6 minutes of ice accretion in Figure 15, the ice shapes show fewer differences than the Appendix C shapes in the previous section. This is because the LWC was the same for all temperatures. Additionally, the horns are more symmetric than for the Appendix C shapes because the AOA was 0° for these simulations. It can also be seen that the ice shapes are smaller for temperatures closer to the freezing point because the freezing fraction is lower for warmer temperatures. The ice shapes that would accrete on an unprotected wing in the same conditions can be seen in Figure A. 10.

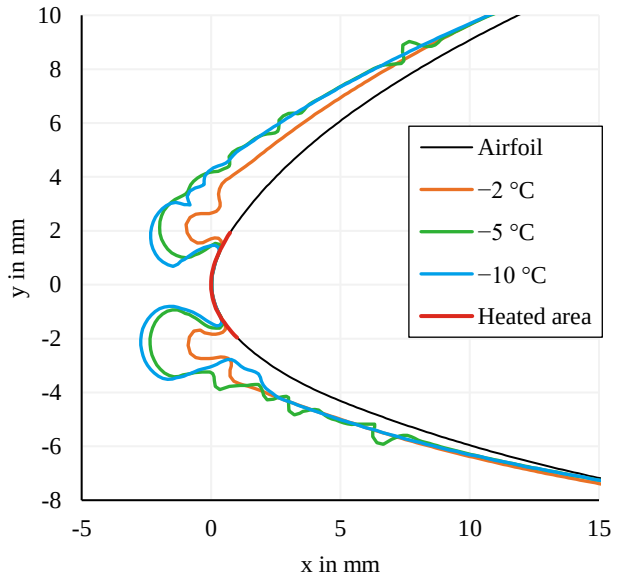

Figure 15: The numerical intercycle ice shapes for the 45 cm wing with a parting strip after 6 minutes of ice accretion for an LWC of 0.44 g/m^3. Airspeed 25 m/s, AOA 0°, 24 µm MVD.

The effect of the changed AOA and the changed Reynolds number can also be seen for the lift and drag coefficients in Figure 16. Both aerodynamic coefficients are significantly lower for the longer wing at the smaller angle of attack. Additionally, the plot shows that the development of the aerodynamic performance differs for the three different temperatures although they have comparable coefficients after 6 minutes of ice accretion. As was observed for the Appendix C cases, the colder ambient temperatures lead to a faster increase in drag and reduction in lift. Since the LWC is the same for all three temperatures, this difference is more significant than for the Appendix C cases.

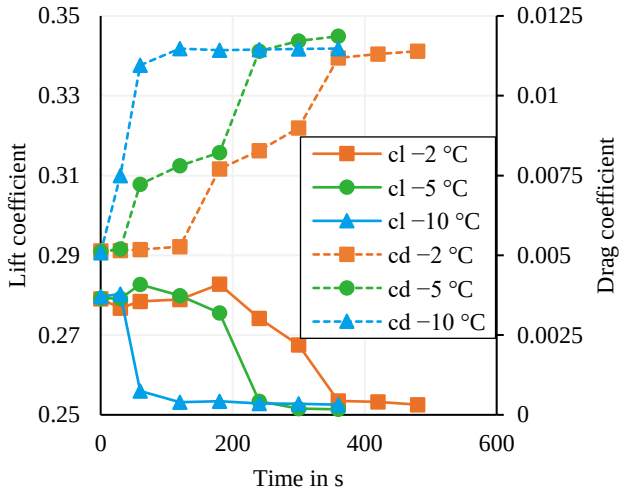

Figure 16: The lift and drag coefficients for intercycle ice shapes with a parting strip for the wing with 0.45 m chord at different temperatures for an LWC of 0.44 g/m^3. Airspeed 25 m/s, AOA 0°, 24 µm MVD.

Following, the drag coefficients are transformed into the time-averaged energy that the engine requires to generate to compensate for the additional drag of the iced airfoils using equations (1) - (4). Depending on the de-icing method, conventional or with a parting strip, the drag coefficient will either be taken from the fully-iced ice shapes or the ice shapes with a parting strip gap. However, as can be seen in Figure 17, the difference in drag coefficient is typically small between the two ice shapes.

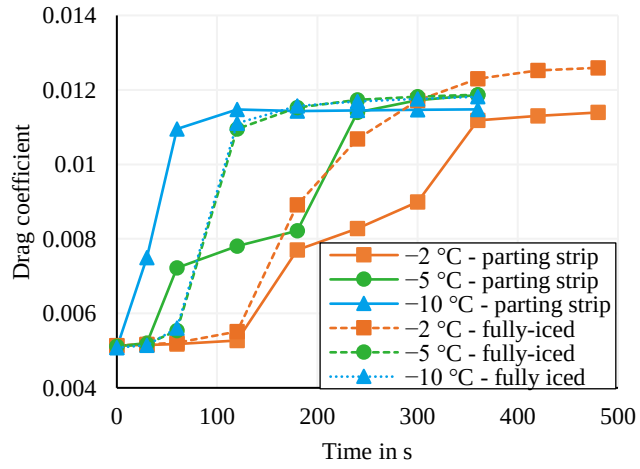

Figure 17: The drag coefficient for different ambient temperatures and ice accretion times for the wing with 0.45 m chord at a LWC of 0.44 g/m^3. Airspeed 25 m/s, AOA 0°, 24 µm MVD. The fully-iced drag coefficients at −5 °C and at −10 °C are almost exactly the same.

Hann et al. [13] provided the required energy for the IPS for different IPS strategies, power modes, and intercycle times. To simplify the following plots of the required energy for the IPS and the drag compensation, only the most energy-efficient IPS power will be shown for every intercycle time.

The required time-averaged energy for different IPS operations at −2 °C is shown in Figure 18 and allows for multiple observations. First, the energy that is required to compensate for the additional intercycle drag is significantly lower than the energy required for the IPS to remove the ice. As a result, also when considering the drag of the intercycle ice, the parting strip de-icing is the most energy-efficient IPS mode followed by conventional de-icing and anti-icing which requires the most energy. However, discussing the energy efficiency of different intercycle times becomes less clear when considering not only the IPS power but also the required thrust. For the case of −2 °C, de-icing with an intercycle time of 4 minutes was more energy-efficient than 6 minutes, while the parting strip de-icing run with 8 minutes was still the most energy-efficient. This is because, on one hand, for longer intercycle times, the IPS becomes typically more energy-efficient as has been shown in different studies [13,14]. On the other hand, more energy is required to compensate for the added drag for longer intercycle times.

Because the energy required to compensate for the intercycle drag is smaller than the energy required for the IPS, flying without any IPS would use the least energy. Assuming the iced aircraft exits the icing conditions after 8 minutes and continues its flight for 4 minutes in non-icing conditions with the added intercycle drag, it would still have used less energy than a UAV using the most energy-efficient IPS mode while flying through the same cloud. Moreover, an aircraft would require approximately the same amount of energy to operate in continuous maximum icing condition of −2 °C, 20 µm MVD, and 0.59 g/m^3 LWC for 1290 s without an IPS as with the most energy-efficient IPS mode as is shown in Figure 18.

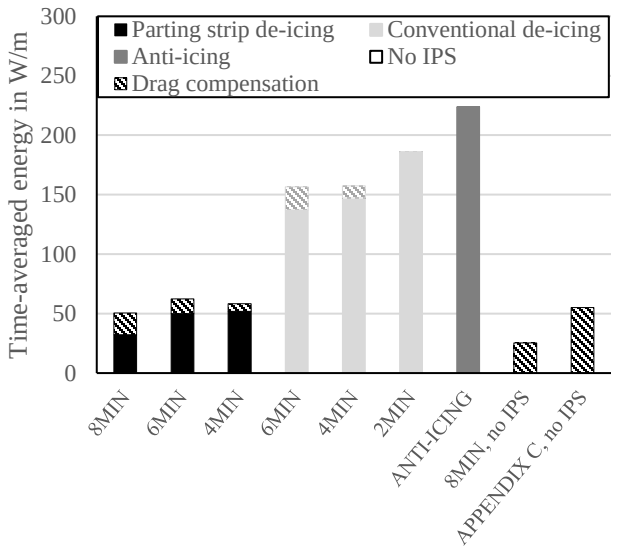

Figure 18: The required time-averaged energy per span for the IPS (filled) and the drag compensation (dashed) for different IPS operations at −2 °C with an LWC of 0.44 g/m^3. In addition, the required energy to compensate the drag of flight in continuous maximum conditions at −2 °C for 1290 s is given. The values are sorted ascending by the required IPS energy. Airspeed 25 m/s, AOA 0°, 24 µm MVD, 0.45 m chord.

The required time-averaged energy at −5 °C for different IPS modes is plotted in Figure 19 and shows the same general characteristics as the plot for the warmer temperature. The biggest difference between −2 °C and −5 °C is the ratio between IPS energy and engine energy for drag compensation. As was shown in Figure 16, the drag coefficient for colder temperatures is slightly higher for the initial period of ice accretion but the difference is not significant. The required IPS energy however changes more significantly for colder temperatures. This is because a larger temperature difference must be overcome to heat the surface above freezing for colder temperatures and because convective cooling is larger for colder temperatures. As

a result, the energy to compensate for additional intercycle drag is less significant for colder temperatures than for warmer temperatures compared to the energy required to shed ice.

Because the influence of the added intercycle drag is smaller for the colder temperature, the flight without any IPS becomes even more energy-efficient than for −2 °C. Assuming the aircraft exits the cloud after 6 minutes and continues flying with the added intercycle drag, it could continue flying for more than 9 minutes outside the icing cloud before using the same energy as the most energy-efficient setting with an IPS.

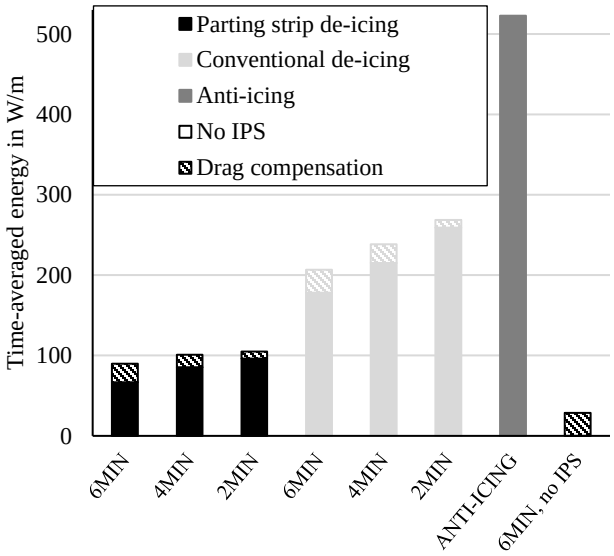

Figure 19: The required time-averaged energy per span for the IPS (filled) and the drag compensation (dashed) for different IPS operations at −5 °C with an LWC of 0.44 g/m^3. The values are sorted ascending by the required IPS energy. Airspeed 25 m/s, AOA 0°, 24 µm MVD, 0.45 m chord.

The difference between the required IPS energy and the drag compensation becomes even more significant for −10 °C as can be seen in Figure 20. This is related to the even larger temperature difference between ambient temperature and freezing temperature, the larger convective cooling, and the comparably smaller increase in drag compared to warmer ambient temperatures. The most energy-efficient IPS technique of the tested ones is conventional de-icing. However, the reason for this could be that the parting strip de-icing was only tested for a shorter intercycle time. The results show that longer intercycle times at −10 °C were more energy-efficient than shorter ones. Additionally, the parting strip de-icing was more energy-efficient than the conventional de-icing with the same intercycle time. This indicates that parting strip de-icing might also be the more energy-efficient method when operating at −10 °C.

Assuming the aircraft exits the cloud after 6 minutes at −10 °C and continues flying with the added drag, it could fly for additional 22 minutes until it has used as much energy as the most energy-efficient method with an IPS. Furthermore, an aircraft would require less energy to operate in continuous maximum icing condition of −10 °C, 20 µm MVD, and 0.42 g/m^3 LWC for 1290 s without an IPS as with the most energy-efficient IPS mode as is shown in Figure 20.

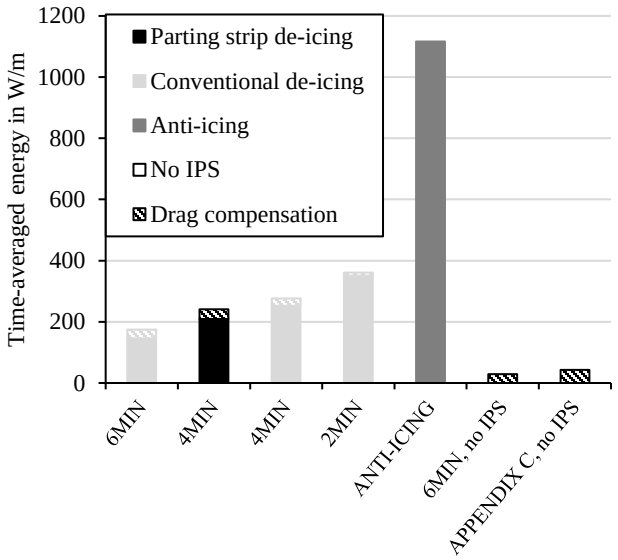

Figure 20: The required time-averaged energy per span for the IPS (filled) and the drag compensation (dashed) for different IPS operations at −10 °C with an LWC of 0.44 g/m^3. In addition, the required energy to compensate the drag of flight in continuous maximum conditions at −10 °C for 1290 s is given. The values are sorted ascending by the required IPS energy. Airspeed 25 m/s, AOA 0°, 24 µm MVD, 0.45 m chord.

Discussion

This study aimed at comparing the energy efficiency of different IPS operations considering both the IPS energy and the energy required to compensate for the added drag caused by iced airfoils.

The Numerical Method

The first step was to compare the ice shapes that develop when heating a parting strip during the flight in icing conditions. The ice shapes were simulated numerically after validating the method with an experimental result. Several assumptions had to be made for the simulations and the simulations had some limitations. Following, the effect of the assumptions and limitations will be discussed.

First, the heat flux was assigned to the wing surface and assumed to be constant over most of the heated area. In real electrothermal IPS applications, the heated material will likely be placed inside the wing and not at the surface [13,39]. This will likely change the heat flux profile at the surface to be less constant. The exact profile will depend on the material used, the size and position of the parting strip, the power provided to the heating zone, and the exact layering of the wing. Second, the heat flux was chosen to be sufficient to not allow any ice accretion. However, the ice horns that develop for longer accretion times catch most of the droplets and fewer droplets impinge in the heated area. Additionally, the convective heat flux is reduced significantly in the heated area because of the reduced wind speed between the two horns. Since heat conduction along the wing surface is not considered in the simulations, the high heat flux at the leading edge results in temperatures exceeding 0 °C significantly and all impinging droplets evaporate, preventing them from running back and freezing downstream. However, since the collection efficiency is small when these unrealistically high temperatures happen, the effect on the resulting ice shapes is considered negligible.

Because the simulations were performed using multi-shot ice accretion, the remeshing of the geometry and the number of shots influence the final ice shapes significantly. A coarser mesh resolution and longer icing shots will both result in ice shapes that appear more round. As a result, the gap between the horns would be reduced, resulting in a closed gap more easily. One shortcoming of the numerical method was that the water film that developed during the previous shot was not considered anymore during the next shot. This could result in underpredicted ice shape sizes in the simulations. The limitations of the simulations also present a challenge in balancing the number of shots between more shots to generate more pointed ice shapes and fewer shots to not lose too much water film during the time of ice accretion.

Finally, numerical simulations of ice accretion typically come with some known limitations. First, most icing simulations assume the ambient conditions to be constant. However, icing conditions can change significantly within a few hundred meters resulting in more complex ice shapes than simulated [40,41]. In addition, ice accretions typically come with significant variance over span and time [23,42] indicating a significant influence of microscopic effects that are not covered by the macroscopic physics solvers used in icing simulations [43]. Remeshing the iced geometry for multi-shot simulations generates an additional problem. Especially for complex geometries with sharp features, the mesh quality can decrease significantly. The comparison between the clean and the iced mesh also showed a worse mesh quality in the leading edge region for the iced geometry than for the clean airfoil. However, creating a mesh with higher quality with the software Pointwise resulted in the same values of lift and drag coefficient for an angle of attack sweep. Hence, the mesh quality is assumed to be sufficient for the purposes of this study.

An additional uncertainty comes with the usage of icing codes for the simulation of icing on unmanned aircraft [44]. Most icing codes are validated using results of manned aircraft that operate at different Reynolds numbers than most UAVs. All these limitations reduce the accuracy of the results.

Icing CFD is typically done using turbulent flow. However, transition was simulated in this study because it was assumed that the clean leading edge might still be in laminar flow in the early stages of ice accretion. If the transition model was unable to correctly predict the onset of transition and larger parts of the airfoil were simulated with laminar flow, the drag coefficient would be underpredicted significantly by the CFD simulations. Since the numerical results indicate that transition happens at the position of the ice horns already after 30 s of ice accretion or latest after 120 s, the assumption of correct prediction of transition onset is considered valid.

An additional assumption of this study was to simulate using a constant airspeed and angle of attack. A real aircraft flying through icing conditions would likely increase either its speed or its angle of attack. This is because the lift that can be generated with iced wings is less than with clean wings. Additionally, the mass of the ice increases the required lift to compensate for the weight of the aircraft. However, the ice mass of the Appendix C shapes after 1290 seconds was less than 0.3 kg for a wingspan of 2 m. While this might be significant for a light aircraft, it only increases the required lift by 1.2% for an aircraft with a weight of 25 kg. To produce the larger lift, the aircraft would need to increase its angle of attack by 0.1° or its airspeed by 0.6%. Moreover, the required increase in angle of attack to maintain a constant lift coefficient at a constant airspeed would be less than 1° for the worst case. Also, the worst aerodynamic degradation would only require an increase of flight speed of 4% to generate enough lift while flying at constant AOA. Hence, it is considered appropriate to simulate with constant airspeed and angle of attack.

The comparison between the numerical intercycle ice shape and the experimental ice shape showed a smaller ice area for the simulation than for the experiment. This could be related to the removal of the water film after every icing shot in the simulation. Additionally, the density of the experimental ice shape might be less than 917 kg/m^3. This would also result in a bigger ice area for the same ice mass. Since the LWC was well calibrated, it is unlikely that the difference in ice shape is related to different LWC values. However, the wind tunnel walls were not included in the numerical grid, potentially changing the effective LWC in the airflow.

Despite all assumptions and shortcomings of icing CFD, the simulated ice shape compares well to the experimental ice shape generated in an icing wind tunnel. Thus, we consider the numerical method to produce good results although the exact values presented in this study include some uncertainty. It must also be noted that three different chord lengths were used in this study. The reason for this is that the required experimental results were only available for slightly longer chord lengths and higher Reynolds numbers than the values intended to be used in the CFD simulations.

Intercycle Ice in Appendix C Conditions

The simulations have shown that using a parting strip has a significant influence on the ice shape. The heated area is kept free from ice and divides the ice shape into two parts. Additionally, the droplets that impact the heated area run back and freeze in unheated areas, resulting in horn shapes aft from the leading edge. The further ice extent is important to consider when designing an ice protection system since it requires the heating zones to extend further downstream as well. A comparison between ice shapes at different ambient temperatures showed that the angle of the horns and the size of the ice gap are mainly influenced by the temperature. The horns start growing in the direction of the incoming flow for cold temperatures, while the horns at warmer temperatures grow normal to the airfoil's surface. A third observation is that the ice horns start growing towards each other in the simulations. This resulted in a closed gap for the coldest simulated temperature. A closed gap would likely decrease the efficiency of parting strip de-icing systems significantly since the aerodynamic forces would no longer shed the ice from the wing. However, the effect of the horns growing together might be overestimated in the simulations because of the remeshing that can result in more rounded shapes. Hence, doing experiments with a parting strip and longer ice accretion times is recommended to further investigate the possibility of a closing ice gap.

Two action points should follow because iced airfoils show a decreased stall angle and lower maximum lift coefficients than clean airfoils. The deteriorated stall behavior will result in a higher stall speed and an increased risk of exceeding the stall angle if the stall warning was chosen for the clean airfoil. First, each aircraft manufacturer that wants to certify his aircraft for flying in icing conditions should evaluate the increase in stall speed because of the deteriorated airfoil performance. If the stall speed for the iced airfoils is too high, the aircraft should use anti-icing during the approach. Second, the manufacturer should adjust the stall warning to the stall angle of the worst realistic ice shape that would accrete on the airfoils for chosen IPS operations.

The development of the lift and drag coefficient over ice accretion time shows a fast deterioration of the airfoil's aerodynamic

performance within the initial period of ice accretion before the change in both coefficients becomes less. This effect can be observed for both, ice shapes with and without the parting strip. For intercycle ice shapes with a parting strip, the deterioration happens typically faster than for ice shapes on unprotected airfoils. This is likely related to the horns that grow faster for ice shapes with a parting strip than for the fully-iced shapes that are more streamlined in the initial period of ice accretion. The horn shapes are also likely to be the reason for the differences between ice shapes at different ambient temperatures. The aerodynamic coefficients deteriorate faster for colder temperatures. This is in line with the horns that grow quicker for colder temperatures because the larger cooling at colder temperatures results in larger freezing fractions. For longer ice accretion times, the lift and drag coefficients become worst for warmer temperatures. This matches the horn geometries that grow more normal to the surface for warmer temperatures and have a larger distance from each other.

An interesting observation can also be made for the stall behavior of the ice shape that developed for larger droplets. Despite being much smaller because of the lower LWC than for smaller droplets, the ice shape results in a smaller stall angle and a reduced maximum lift coefficient compared to the ice shape for smaller droplets. Comparing the lift coefficients of ice shapes after a flight in the same conditions for different durations also shows a reduced stall angle for short durations of ice accretion. This supports the importance of the horn geometries on the stall behavior of the airfoil. Additionally, this indicates that smaller intercycle ice shapes can be worse for the stall behavior of the aircraft than larger ice shapes accreted in the same icing conditions.

The Required Energy for Flight in Icing Conditions

While the changes in lift coefficient are rather small for moderate angles of attack, the drag coefficient shows significant changes. It can double within less than three minutes of ice accretion. Thus, the aircraft requires more thrust to maintain steady flight operation. A complete investigation of the required energy for the flight of a UAV in icing conditions must combine the energy required for the IPS and the energy required to increase the thrust of the aircraft. For this study, the required motor energy to compensate for the added drag of simulated ice shapes and the required IPS energy for experimental ice shedding are calculated.

Several assumptions were made during the calculation of the required energy. First, as discussed and quantified before, the required changes in airspeed and angle of attack are considered negligible. Flying with the added mass on the wings and the reduced lift coefficient could require an increase in angle of attack by 1° or in airspeed by 4%. These changes would also increase the drag coefficient by 10-20% for an ice accretion duration of 1290 s. While this would increase the required engine energy to produce enough thrust, the effects are significantly smaller than the required engine energy to compensate the intercycle drag that increases by 150-200% for the same duration. Second, the study assumes that the IPS is stopped immediately when shedding happens. In real flight applications, even if the aircraft is equipped with a shedding detector [45], the IPS would likely heat for a slightly longer period, increasing the energy used per de-icing cycle. Since this depends heavily on the shedding time and the shedding detection time, it is difficult to quantify but delayed shedding detection could easily increase the required IPS power by 20-30% for shedding times of 10 s. Hence, when including the additional drag because of increasing the angle of attack and the longer heating period than the shedding time, it is likely that both effects are in the same order of magnitude. Third, because of the availability of experimental data, the energy calculations were performed for an AOA of 0°. In real flight, the aircraft must operate at a larger angle of attack to produce enough lift. Larger angles of attack also generate more drag. However, this study only considers the difference in drag between an iced aircraft and a clean aircraft. The amount of intercycle drag varies only by approximately 10% between 0° AOA and 4°. Hence, this assumption is considered acceptable. Fourth, the drag increase is only calculated until the de-icing was started, resulting in an assumption of immediate shedding after activation of the de-icing system. Because shedding typically happens within seconds and hence, within a much short time than the icing duration, this assumption is considered acceptable for this study. Fifth, the study considers the drag to be equal to the clean airfoil after the ice has shed. This neglects the influence of runback icing and other ice residuals. Further investigations are required to investigate the influence of runback icing and other ice residuals after shedding. Additionally, the study assumes no runback icing for the anti-icing operation for the same reason. Finally, the study only considers added drag because of ice accretion on wings and the IPS power required to protect the wings. Other parts of the aircraft, for example icing on the empennage [46], are not included in the study.

Some recommendations for the operation of IPS systems and future work can be drawn from this study. First, it has been shown that even when considering the energy required to compensate for the drag of intercycle ice shapes, parting strip de-icing is more energy-efficient than conventional de-icing, while anti-icing remains the least energy-efficient IPS method. Second, it has been shown that the required energy for an IPS is typically significantly larger than the required energy to compensate for drag. Hence, finding the IPS operation that uses the least time-averaged energy is more important than including the drag of the intercycle ice shape. This also indicates the importance of optimizing the IPS design and operation for energy efficiency. Third, especially for colder temperatures, longer intercycle times were typically more energy-efficient. However, this finding requires some additional considerations or additional work. For example, this study showed that the two horns grow closer to each other for longer ice accretion times and might even grow into each other. This would change the de-icing operation into conventional de-icing even if the IPS uses a parting strip and reduce the energy efficiency significantly as shown in this study. Additionally, longer intercycle times increase the required thrust. For this study, it was assumed that the engine and propeller can provide any thrust that is required. This is not true for real flight applications, especially because the propeller will also be iced. As a result, the propeller will produce less thrust and require an IPS itself [3,47]. Hence, the possible intercycle times might be limited by the time until the horns grow too close to each other and by the maximum thrust that the propeller can produce in icing conditions. As this study has shown, the required thrust increases fast within the initial period of ice accretion. This might require very short de-icing intervals to stay within the thrust limits that the propeller can deliver.

Hence, a more comprehensive study of the most energy-efficient flight of an unmanned aircraft in icing conditions would require considering the added drag of intercycle ice shapes, the IPS power to protect the wings, the IPS power to protect the propeller, and the thrust that can be produced by the propeller in icing conditions.

This study indicates that, when only optimizing for the energy usage, it might be the most energy-efficient to only de-ice the wings after the icing cloud has been exited. However, several other parameters must be considered when optimizing the IPS. First, the stall angle of iced airfoils is significantly lower than the stall angle of a clean

airfoil. As a result, when the aircraft must increase the angle of attack to compensate for reduced lift coefficient and increased mass, it can operate in stall. The risk of exceeding the stall angle would be particularly large for descend. Hence, the wings should be de-iced before starting to descend and it should be considered to use anti-icing during descend in icing conditions to operate below the stall angle. Second, maneuverability has not been considered during this study. It is likely that the ice accretions would reduce the flyability of the aircraft significantly and hence, the maximum intercycle time might be limited by the maximum degradation in flight stability that can be handled by the aircraft and a possible autopilot.

Summary

This paper presents numerical results on the aerodynamic performance of airfoils in icing conditions. Iced airfoils with and without a parting strip are compared with a clean airfoil. The results show that iced airfoils are worse in aerodynamic performance than clean airfoils. Additionally, iced airfoils with a parting strip show slightly worse aerodynamics than iced airfoils without a parting strip. The biggest aerodynamic degradation of intercycle ice shapes happens in the stall area. Both, the stall angle and the maximum lift coefficient are reduced compared to the clean airfoil. The aerodynamic performance is worse for temperatures closer to the freezing point, likely related to the horns that grow more normal to the airflow for warmer temperatures.

The study also showed that the deterioration of aerodynamic coefficients happens faster in the initial period of ice accretion and more slowly later. The effect is more significant for colder temperatures where larger freezing fractions result in faster growth of horns compared to warmer temperatures.

The goal of this study was to evaluate the energy efficiency of different IPS operations in icing conditions. Extending from previous research, not only the energy required for the IPS was considered but also the energy to compensate for the higher drag caused by the iced wings. The results showed that parting strip de-icing is still the most energy-efficient method of an IPS even when including the larger thrust requirements. Additionally, the study showed that the energy requirements for the IPS exceed the energy requirements for the thrust significantly. The difference is larger for colder temperatures because of the larger difference between ambient temperature and the melting temperature of ice.

In fact, the study showed that not using an IPS might be the most energy-efficient operation, especially for cold temperatures. This is because the IPS requires significantly more energy than is required to compensate for the additional intercycle drag. However, this result does not consider that the maneuverability will be reduced significantly by iced airfoils and that the risk of operating in stall conditions is increased when flying with iced airfoils.

The study provided important knowledge on the energy efficiency of different IPS operations for UAVs. The results can for example be used to improve the quality of path planners. Moreover, the findings of the study highlight the importance of developing more energy-efficient ice protection systems for UAVs to enable the safe operation of UAVs in icing conditions without reducing the endurance and range significantly.

References

[1] Hann, R., and Johansen, T., “Unsettled Topics in Unmanned Aerial Vehicle Icing,” SAE Edge Report, 2020, doi: 10.4271/epr2020008.

[2] Liu, Y., Li, L., Chen, W., Tian, W., and Hu, H., “An Experimental Study on the Aerodynamic Performance Degradation of a UAS Propeller Model Induced by Ice Accretion Process,” *Experimental Thermal and Fluid Science*, Vol. 102, 2019, pp. 101–112, doi: 10.1016/j.expthermflusci.2018.11.008.

[3] Müller, N. C., and Hann, R., “UAV Icing: A Performance Model for a UAV Propeller in Icing Conditions,” *AIAA AVIATION 2022 Forum*, 2022, doi: 10.2514/6.2022-3903.

[4] Løw-Hansen, B., Coates, E. M. L., Müller, N. C., Johansen, T. A., and Hann, R., “Identification of an Electric UAV Propulsion System in Icing Conditions,” *Manuscript submitted for publication*, 2023.

[5] Cao, Y., Tan, W., and Wu, Z., “Aircraft Icing: An Ongoing Threat to Aviation Safety,” *Aerospace Science and Technology*, Vol. 75, 2018, pp. 353–385, doi: 10.1016/j.ast.2017.12.028.

[6] Bragg, M. B., Broeren, A. P., and Blumenthal, L. A., “Iced-Airfoil Aerodynamics,” *Progress in Aerospace Sciences*, Vol. 41, No. 5, 2005, pp. 323–362, doi: 10.1016/j.paerosci.2005.07.001.

[7] Thomas, S. K., Cassoni, R. P., and MacArthur, C. D., “Aircraft Anti-Icing and De-Icing Techniques and Modeling,” *Journal of Aircraft*, Vol. 33, No. 5, 1996, pp. 841–854, doi: 10.2514/3.47027.

[8] Henry, R., “Development of an Electrothermal De-Icing/Anti-Icing Model,” *30th Aerospace Sciences Meeting & Exhibit*, AIAA 92-0526, 1992.

[9] Siquig, R. A., “Impact of Icing on Unmanned Aerial Vehicle (UAV) Operations,” Naval Environmental Prediction Research Facility Report, 1990.

[10] Hann, R., and Wallisch, J., “UAV Database,” *DataverseNo, Version 1*, 2020, doi: 10.18710/L41IGQ.

[11] Hann, R., and Johansen, T. A., “UAV Icing: The Influence of Airspeed and Chord Length on Performance Degradation,” *Aircraft Engineering and Aerospace Technology*, Vol. 93, No. 5, 2021, pp. 832–841, doi: 10.1108/AEAT-06-2020-0127.

[12] Szilder, K., and McIlwain, S., “In-Flight Icing of UAVs - The Influence of Reynolds Number on the Ice Accretion Process,” SAE Technical Paper 2011-01-2572, 2011, doi: 10.4271/2011-01-2572.

[13] Hann, R., Enache, A., Nielsen, M. C., Stovner, B. N., van Beeck, J., Johansen, T. A., and Borup, K. T., “Experimental Heat Loads for Electrothermal Anti-Icing and De-Icing on UAVs,” *Aerospace*, Vol. 8, No. 3, 2021, doi: 10.3390/aerospace8030083.

[14] Wallisch, J., and Hann, R., "UAV Icing: Experimental Investigation of Ice Shedding Times with an Electrothermal De-Icing System," *AIAA AVIATION 2022 Forum*, 2022, doi: 10.2514/6.2022-3905.

[15] Hann, R., Borup, K., Zolich, A., Sorensen, K., Vestad, H., Steinert, M., and Johansen, T., "Experimental Investigations of an Icing Protection System for UAVs," *SAE Technical Paper 2019-01-2038*, 2019, doi: 10.4271/2019-01-2038.

[16] Enache, A., Bernay, B., Glabeke, G., Planquart, P., and van Beeck, J., "Ice Shedding Phenomenon: An Experimental and Numerical Investigation," *AIAA AVIATION 2020 FORUM*, 2020.

[17] Pourbagian, M., and Habashi, W. G., "Aero-Thermal Optimization of in-Flight Electro-Thermal Ice Protection Systems in Transient de-Icing Mode," *International Journal of Heat and Fluid Flow*, Vol. 54, 2015, pp. 167–182, doi: 10.1016/j.ijheatfluidflow.2015.05.012.

[18] Frimann Loes Narum, E., Hann, R., and Arne Johansen, T., "Optimal Mission Planning for Fixed-Wing UAVs with Electro-Thermal Icing Protection and Hybrid-Electric Power Systems," *2020 International Conference on Unmanned Aircraft Systems, ICUAS 2020*, 2020.

[19] Cheung, M., and Hann, R., "UAV Icing: Icing Scenarios for Validation of Particle Swarm Path Planning Method," *Manuscript submitted for publication*, 2023.

[20] Ozcer, I., Switchenko, D., Baruzzi, G. S., and Chen, J., "Multi-Shot Icing Simulations with Automatic Re-Meshing," *SAE Technical Papers*, Vols. 2019-June, No. June, 2019, pp. 1–15, doi: 10.4271/2019-01-1956.

[21] Beaugendre, H., Morency, F., and Habashi, W. G., "Development of a Second Generation In-Flight Icing Simulation Code," *Journal of Fluids Engineering, Transactions of the ASME*, Vol. 128, No. 2, 2006, pp. 378–387, doi: 10.1115/1.2169807.

[22] Tran, P., Baruzzi, G., Tremblay, F., Benquet, P., Habashi, W. G., Petersen, P. B., Liggett, M. W., and Fiorucci, S., "FENSAP-ICE Applications to Unmanned Aerial Vehicles (UAV)," *AIAA Paper*, 2004.

[23] Hann, R., "UAV Icing: Ice Accretion Experiments and Validation," *SAE Technical Paper 2019-01-2037*, 2019, doi: 10.4271/2019-01-2037.

[24] Chung, J. J., and Addy, H. E., "A Numerical Evaluation of Icing Effects on a Natural Laminar Flow Airfoil," *38th Aerospace Sciences Meeting and Exhibit*, 2000.

[25] ANSYS Inc., "Ansys FENSAP-ICE User Manual," 2022.

[26] Tiihonen, M., Jokela, T., Makkonen, L., and Bluemink, G.-J., "VTT Icing Wind Tunnel 2.0," *Winterwind Presentations*, 2016.

[27] Hann, R., Müller, N. C., Lindner, M., and Wallisch, J., "UAV Icing: Experimental Validation Data for Predicting Ice Shapes at Low Reynolds Numbers," *Manuscript submitted for publication*, 2023.

[28] Chang, H.-P., Kimble, K. R., Frost, W., and Shaw, R. J., "Influence of Multidroplet Size Distribution on Icing Collection Efficiency," *AIAA 21st Aerospace Sciences Meeting*, 1983, doi: 10.2514/6.1983-110.

[29] Langmuir, I., and Blodgett, K. B., "A Mathematical Investigation of Water Droplet Trajectories," 1946.

[30] Federal Aviation Administration, "Appendix C to 14 CFR 25 and 29. Part I - Atmospheric Icing Conditions," Docket No. 5066, 29 FR 18291, 1964.

[31] Hann, R., Hearst, R. J., Sætran, L. R., and Bracchi, T., "Experimental and Numerical Icing Penalties of an S826 Airfoil at Low Reynolds Numbers," *Aerospace*, Vol. 7, No. 4, 2020, doi: 10.3390/aerospace7040046.

[32] Fajt, N., Hann, R., and Lutz, T., "The Influence of Meteorological Conditions on the Icing Performance Penalties on a UAV Airfoil," *8th European Conference for Aeronautics and Space Sciences (EUCASS)*, 2019, doi: 10.13009/EUCASS2019-240.

[33] Selig, M. S., Gugliemo, J. J., Broeren, A. P., and Giguère, P., "Summary of Low-Speed Airfoil Data," SoarTech Publications, Virginia Beach, 1995.

[34] Croce, G., De Candido, E., Habashi, W. G., Aubé, M. S., and Baruzzi, G. S., "FENSAP-ICE: Numerical Prediction of in-Flight Icing Roughness Evolution," *1st AIAA Atmospheric and Space Environments Conference*, 2009, doi: 10.2514/6.2009-4126.

[35] Ozcer, I. A., Baruzzi, G. S., Reid, T., Habashi, W. G., Fossati, M., and Croce, G., "FENSAP-ICE: Numerical Prediction of Ice Roughness Evolution, and Its Effects on Ice Shapes," *SAE Technical Papers*, 2011, doi: 10.4271/2011-38-0024.

[36] Anderson, J. D., "Fundamentals of Aerodynamics.," McGraw Hill, New York, NY, 2016.

[37] Gong, A., Macneill, R., and Verstraete, D., "Performance Testing and Modeling of a Brushless Dc Motor, Electronic Speed Controller and Propeller for a Small Uav," *2018 Joint Propulsion Conference*, 2018.

[38] Merchant, M. P., and Miller, L. S., "Propeller Performance Measurement for Low Reynolds Number UAV Applications," *Collection of Technical Papers - 44th AIAA Aerospace Sciences Meeting*, No. 18, 2006.

[39] AI-Khalil, K. M., Horvath, C., Miller, D. R., and Wright, W. B., "Validation of Nasa Thermal Ice Protection Computer Codes Part 3-the Validation of Antice," *35th Aerospace Sciences Meeting and Exhibit*, 1997.

[40] Bernstein, B. C., McDonough, F., Politovich, M. K., Brown, B. G., Ratvasky, T. P., Miller, D. R., Wolff, C. A., and Cunning, G., "Current Icing Potential: Algorithm Description and Comparison with Aircraft Observations," *Journal of Applied Meteorology*, Vol. 44, No. 7, 2005, doi:

10.1175/JAM2246.1.

[41] Hansman, R. J., “The Influence of Ice Accretion Physics on the Forecasting of Aircraft Icing Conditions,” 1989.

[42] SAE International, “Icing Wind Tunnel Interfacility Comparison Tests,” Aerospace Information Report AIR5666, 2012.

[43] Bansmer, S. E., “Aircraft Icing. A Challenging Problem of Fluid Mechanics.,” CUVILLIER VERLAG, 2019.

[44] Hann, R., “UAV Icing: Challenges for Computational Fluid Dynamic (CFD) Tools,” *International Conference on Computational Fluid Dynamics (ICCFD11)*, 2022.

[45] Løw-Hansen, B., Hann, R., and Johansen, T. A., “UAV Icing: Ice Shedding Detection Method for an Electrothermal De-Icing System,” *AIAA AVIATION 2022 FORUM*, 2022.

[46] Lindner, M., Wallisch, J., and Hann, R., “UAV Icing: Numerical Simulation of Icing Effects on Wing and Empennage,” *Manuscript submitted for publication*, 2023.

[47] Müller, N. C., and Hann, R., “UAV Icing: 3D Simulations of Propeller Icing Effects and Anti-Icing Heat Loads.,” *Manuscript submitted for publication*, 2023.

Contact Information

Joachim Wallisch, joachim.wallisch@ntnu.no

Richard Hann, richard.hann@ntnu.no

Acknowledgments

The authors thank Tuomas Jokela, Mikko Tiihonen, and Jennifer Carreiro Spencer from VTT for their support in conducting the experiments in the icing wind tunnel. Furthermore, we thank Maritime Robotics and UBIQ Aerospace for providing access to the airfoil used in the experimental tests, and Shaoquan Wang (UBIQ Aerospace) for preparing the wing with the parting strip.

The work is partly sponsored by the Research Council of Norway through the Centre of Excellence funding scheme, project number 223254, AMOS, the IPN Pathplanning project with project number 318000, and the IKTPLUSS project with project number 316425.

Parts of the numerical simulations were performed on the resources provided by the National Infrastructure for High Performance Computing and Data Storage in Norway (UNINETT Sigma2) on the Fram supercomputer, under project number NN9613K Notur/NorStore.

Appendix

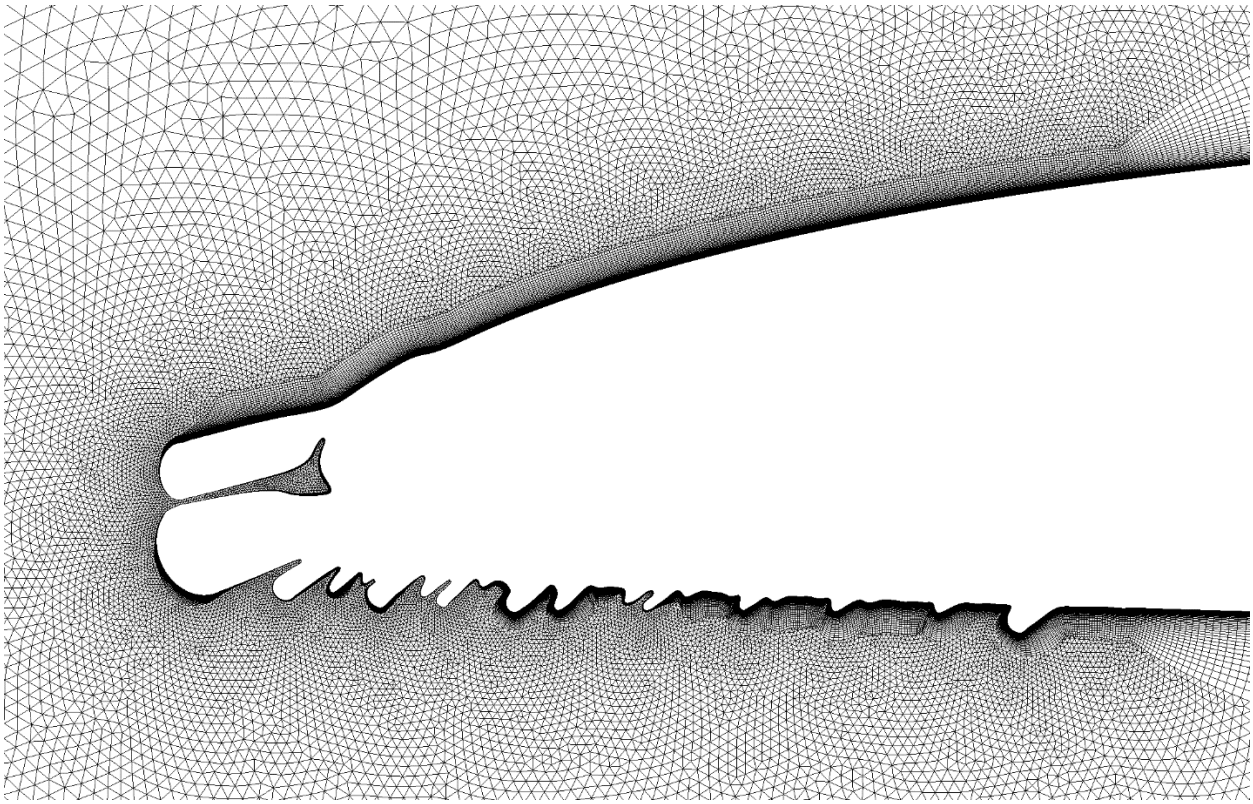

Figure A. 1: A close-up view of the hybrid mesh around the leading edge of an iced airfoil.

Table A. 1: An overview of all numerical settings used for the CFD simulations.

Setting	Value
Software	ANSYS FENSAP-ICE 2022 R2
2-D or 3-D?	2.5-D (one cell in spanwise direction)
Turbulence model	k-ω-SST
Transition	Simulated with the intermittency model
Gravity	Included with 9.81 kg/(ms^2)
Steady or unsteady?	Multi-shot (multiple steady simulations)
Duration of shots (Appendix C)	1 x 30 seconds + 14 x 90 seconds
Duration of shots (Shorter simulations)	2 x 30 seconds + 60 second steps (Amount depending on total duration)
Artificial viscosity	Second order streamline upwind
Droplet size	Monodisperse
Ice density	917 kg/m^3

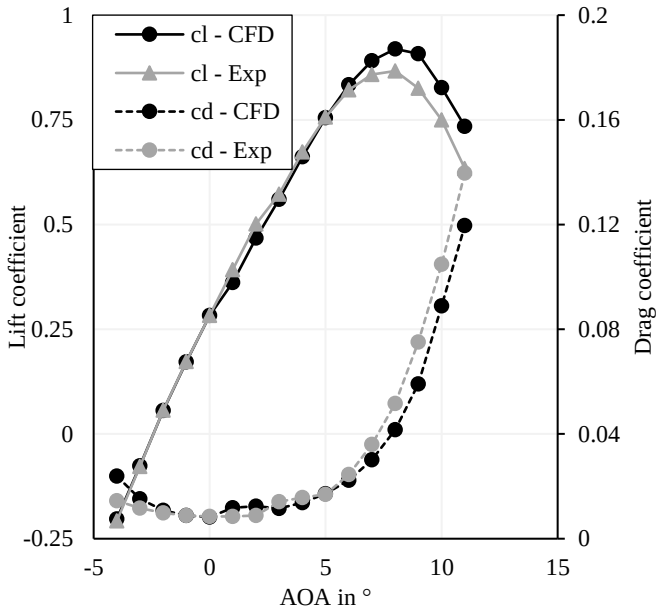

Figure A. 2: The lift coefficient c_l and the drag coefficient c_d for the numerical ("CFD") and the experimental ("Exp") ice shapes that accreted at −5 °C after 240 s of icing with LWC = 0.44 g/m^3 on a wing with 0.35 m chord and a heated parting strip. Airspeed 25 m/s, MVD 24 µm, AOA 0°.

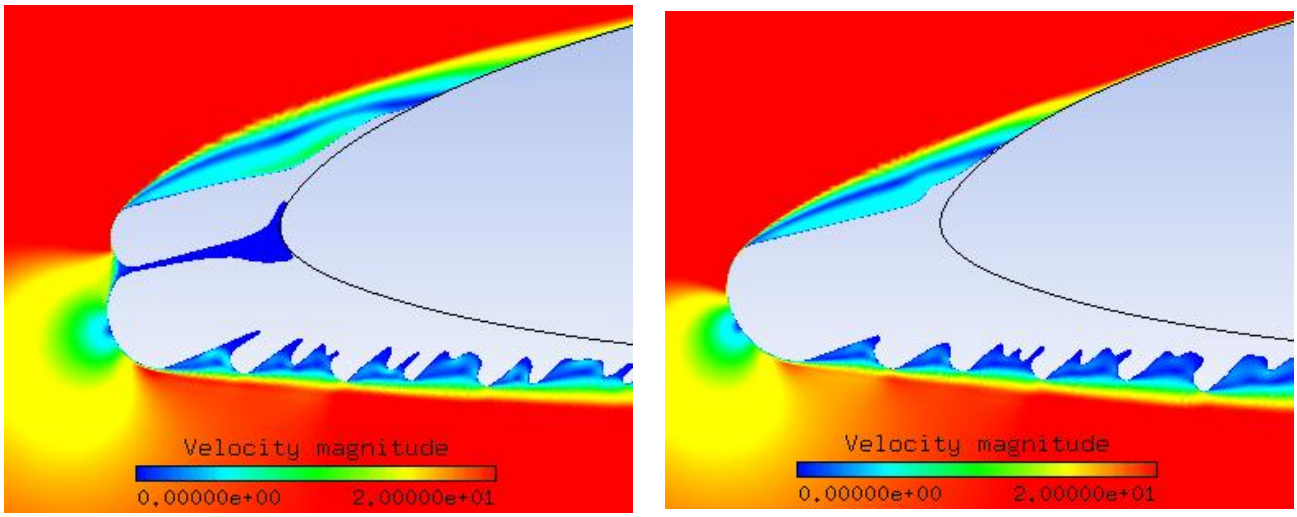

Figure A. 3: The velocity for intercycle ice shapes after 1290 s of icing at −5 °C, 0.53 g/m^3 LWC, and 20 µm MVD. An ice shape with a parting strip gap on the left, and a fully-iced shape on the right. The different pictures indicate the further extend of the separation on the suction side for the ice shape with parting strip. Airspeed 25 m/s, 0.3 m chord, AOA 4°.

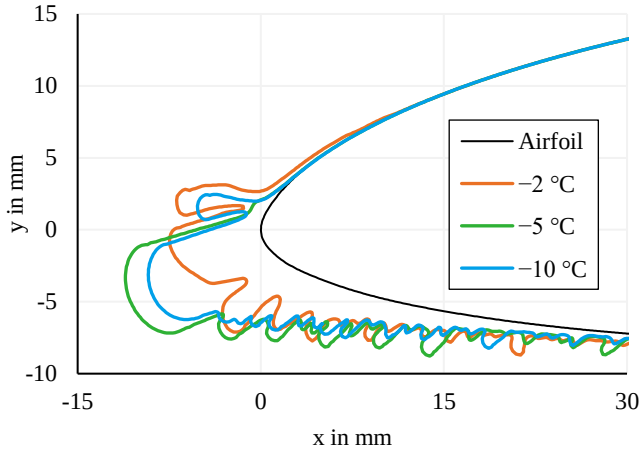

Figure A. 4: The intercycle ice shapes on an unprotected airfoil with 0.3 m chord length for different temperatures after 1290 seconds of ice accretion in continuous maximum conditions for an MVD of 20 µm. Airspeed 25 m/s, AOA 4°.

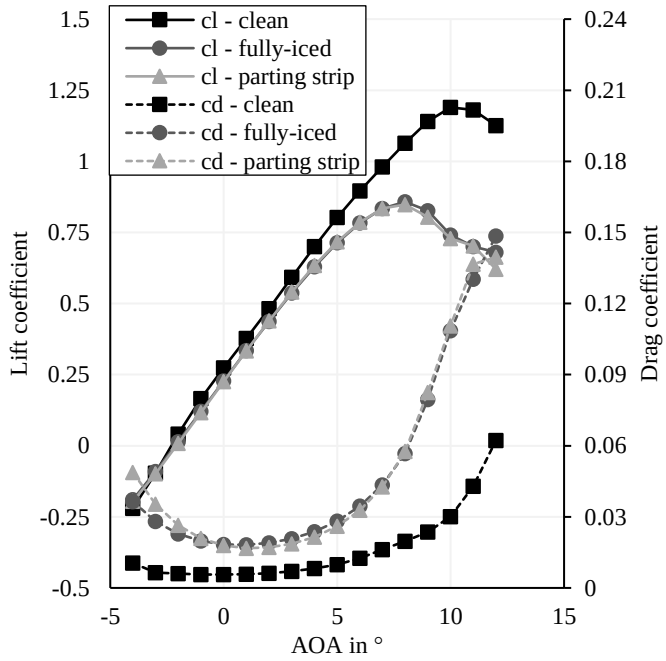

Figure A. 5: The plots of the lift coefficient c_l and the drag coefficient c_d for a clean airfoil, an iced airfoil without a parting strip, and an iced airfoil with a parting strip. The coefficients of the iced airfoils are for 1290 seconds long icing encounters at −2 °C, 0.59 g/m^3 LWC, and 20 µm MVD with an AOA of 4°. Airspeed 25 m/s, 0.3 m chord.

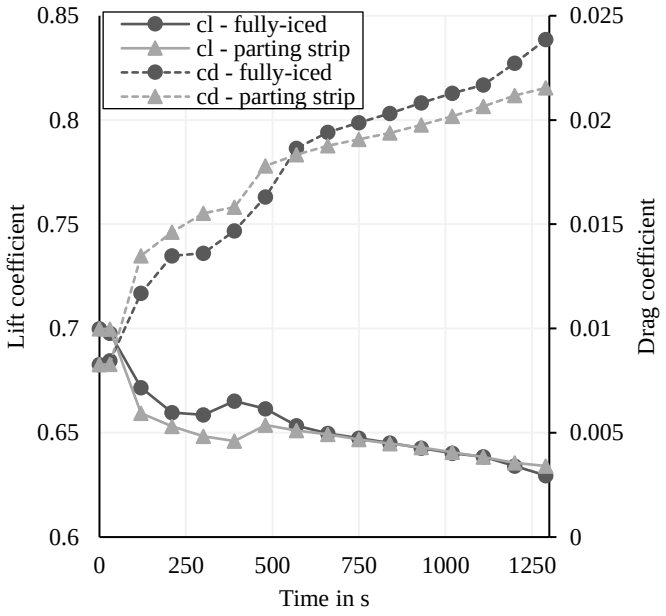

Figure A. 6: The lift coefficient c_l and the drag coefficient c_d for a fully-iced airfoil and an iced airfoil with a parting strip for different durations of icing encounters at −2 °C, 0.59 g/m^3 LWC, and 20 µm MVD. Airspeed 25 m/s, 0.3 m chord, AOA 4°.

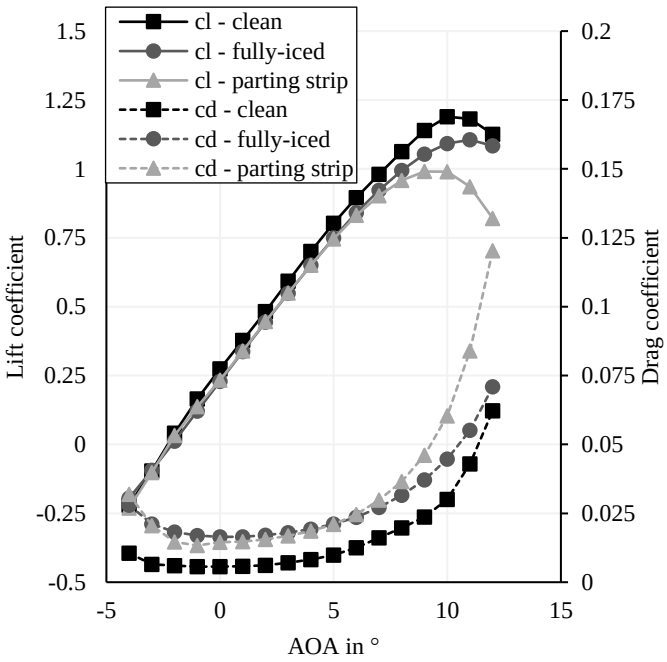

Figure A. 7: The plots of the lift coefficient c_l and the drag coefficient c_d for a clean airfoil, an iced airfoil without a parting strip, and an iced airfoil with a parting strip. The coefficients of the iced airfoils are for 1290 seconds long icing encounters at −10 °C, 0.42 g/m^3 LWC, and 20 µm MVD with an AOA of 4°. Airspeed 25 m/s, 0.3 m chord.

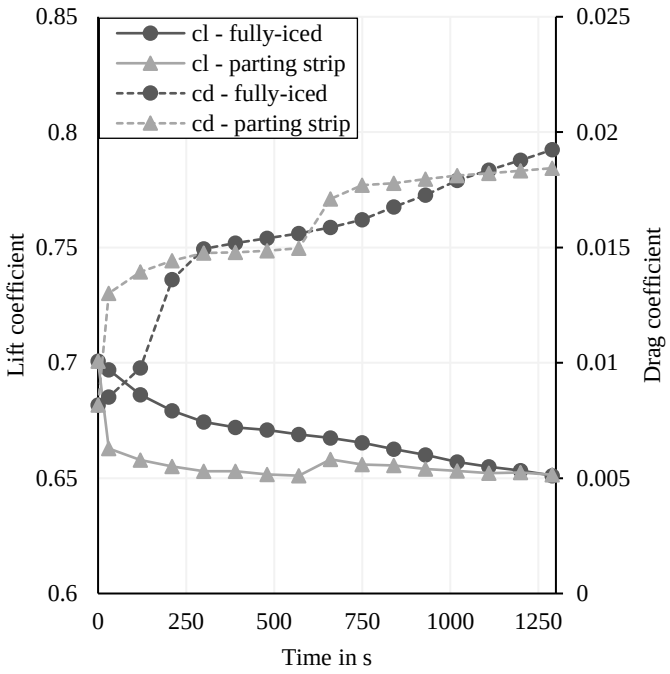

Figure A. 8: The lift coefficient c_l and the drag coefficient c_d for a fully-iced airfoil and an iced airfoil with a parting strip for different durations of icing encounters at −10 °C, 0.42 g/m^3 LWC, and 20 µm MVD. Airspeed 25 m/s, 0.3 m chord, AOA 4°.

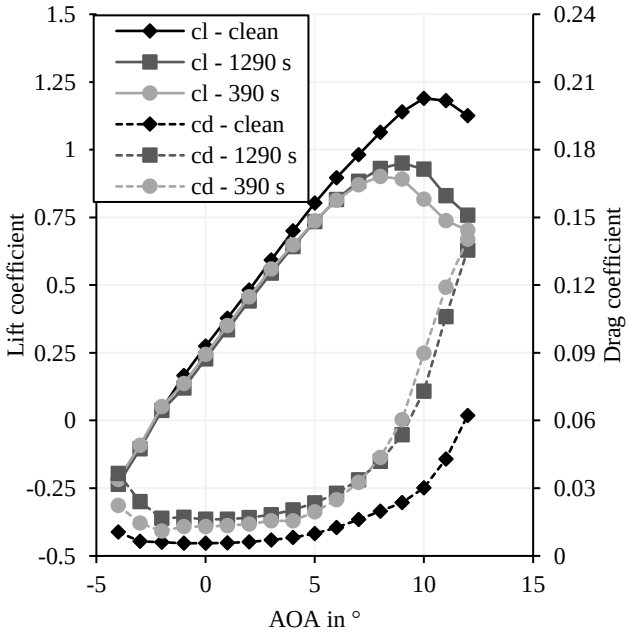

Figure A. 9: The plots of the lift coefficient c_l and the drag coefficient c_d for a clean airfoil and iced airfoils with a parting strip after different durations of icing at −5 °C, 0.53 g/m^3 LWC, and 20 µm MVD with an AOA of 4°. Airspeed 25 m/s, 0.3 m chord.

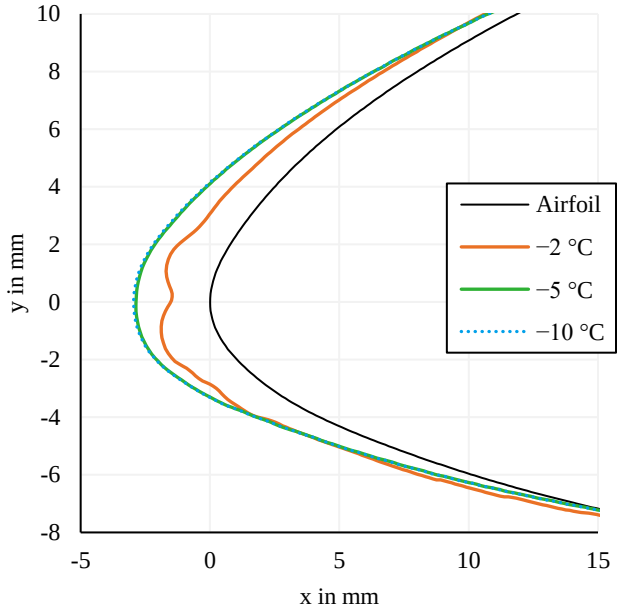

Figure A. 10: The numerical intercycle ice shapes for the unprotected 45 cm wing after 6 minutes of ice accretion for an LWC of 0.44 g/m^3. Airspeed 25 m/s, 24 µm MVD, AOA 0°. The ice shapes at −5 °C and at −10 °C are almost exactly similar.